Title	Pressure-induced metallic phase of hydrogen-rich systems
Author(s)	Nguyen, Huyen Thi Le
Citation	大阪大学, 2012, 博士論文
Version Type	VoR
URL	https://hdl.handle.net/11094/26848
rights	
Note	

Pressure-induced metallic phase of hydrogen-rich systems

Nguyen Thi Le Huyen

March 2012

Pressure-induced metallic phase of hydrogen-rich systems

A dissertation submitted to
The Graduate School of Engineering Science
OSAKA UNIVERSITY

in partial fulfillment of the requirements for the degree of
DOCTOR OF PHILOSOPHY IN SCIENCE

by

Nguyen Thi Le Huyen

March 2012

Abstract

Solid hydrogen was predicted to be metallic and even a room-temperature superconductor under very high pressure. The pressure is predicted to be so enormous exceeding 400 GPa [1], which is still out of range for experimentalists. Hence, the pressurized hydrogen-rich materials are expected as alternative approach which may offer a great promise that could be a so-called "chemical pre-compression" from the metal atoms combining additional pressure, facilitating hydrogen densities in the range where the metallization could occur. Two systems are focused in this thesis. The first system is YH_3 and the second is perovskite hydrides $CaCoH_3$ and $CaNiH_3$. Relatively high volumetric hydrogen content are expected in both sample to emerge at pressure accessible in a diamond-anvil cell.

- Yttrium can form a hydride able to absorb about 300 mol% hydrogen, which is a yellowish transparent insulator with hcp-structured YH_3 at ambient pressure. The band gap is very large with 2.8 eV [2]. From a study of the optical properties at ambient pressure, the semiconductor gap remains open until at least 25 GPa. Further extrapolating the pressure dependence of the gap, an insulator to metal (I-M) transition is expected at 55 ± 8 GPa [3]. A theoretical prediction indicated the occurrence of pressure-induced superconductivity with T_c of 40 K at 17.7 GPa in the high-pressure fcc phase of YH_3 [4]. We focus our attention to unravel the metallization in YH_3 via electrical resistance measurement under high pressure and low temperature. We have succeeded in synthesized the insulating transparent YH_3 samples by hydrogenation from yttrium metal in fluid H_2 under high pressure. Measurement of the electrical resistivity at high pressure and low temperature demonstrated an electronic phase transition from insulator to metal at around 70 GPa in the fcc phase.

- The cubic perovskite-type ABH_3 comprised of a divalent metal (A) and a transition metal (B) exhibit a variable degree of hydrogen deficiency, but the ideal perovskite structure is stable at ambient pressure [5]. However, the possibility to induced I-M transition by applying pressure of perovskite-type hydride has never been considered. This hydride correlate with the characteristics of the transition metal d-band, the 4s band may lie between the localized 3d-like states. There are perovskite hydrides $CaCoH_3$ and

$CaNiH_3$. Both samples reveal that the cubic perovskite phase is found to be stable in a wide range of high pressure, and no structure phase transition at room temperature to 62 GPa and 83 GPa, respectively. The I-M transition at high pressure in $CaT\text{-}H_3$ for T = Ni, Co were found. In $CaCoH_3$, the negative slope of $d\rho/dT$ manifests the non-metallic behavior at 17 GPa. Upon increasing the pressure, above 40 GPa the $d\rho/dT$ slope reversed to positive, leading support to the occurrence of metallization. In the case of $CaNiH_3$, the onset pressure of metallization is 15 GPa. However, the superconductivity was not observed yet up to 80 GPa in both samples.

These results could be an important step towards understanding underlying physics of superconducting metallic hydrogen-rich systems which a new system to study high temperature superconductivity.

Document structure

This document consists of five chapters. The various chapters are further divided into sections and subsections. Chapter 1 outlines the background for this work. Chapter 2 gives a description of the experimental setup. The experimental results and discussions are given in Chapter 3 and 4 and the conclusions with some recommendations for future work are presented in Chapter 5.

Reference

[1] E. Wigner *et al.*, J. Chem. Phys 3: 764–770 (1935), N. W. Ashcroft, Phys. Rev. Lett., 21, 1748 (1968).

[2] A. Ohmura *et al.*, Appl. Phys. Lett., 91, 151904 (2007).

[3] R. J. Wijngaarden *et al.*, J. Alloys and Compounds, 308 (2000) 44-48.

[4] D.Y. Kim *et al.*, Phys. Rev. Lett., 103 (2009) 077002.

[5] R. H. Mitchell *et al.*, Mineralogical Magazine, April 2003, v. 67, p. 419-420.

CONTENT

Chapter 1. Introduction

Hydrogen is one of the basic materials in science, and many major discoveries have been made from studies of atomic and molecular hydrogen. In more than half a century since, the predicted pressure for the metallization has risen from 25 GPa to 600 GPa regions. Metallic hydrogen has not been yet found at these pressures. This chapter mainly covers the trials for the creation of "metallic hydrogen" in the experimental research, which is one of the principal goals of high-pressure research.

1.1 High pressure

Pressure is one of the fundamental thermodynamic variables, which can be varied over range of more than sixty orders of magnitude, from the vacuum of outer space to pressures in the interior of neutron stars. The study of the behavior of materials at high pressures and low temperatures has been useful not only in understanding the properties of these materials but also in the observation of new features of the physicochemical properties; therefore a combination of high pressures with low temperatures is a logical step in pursuing this phenomenon.

It is now believed that almost all materials will become metallic at sufficiently high pressures. To examine materials under extreme pressures, we often use a device called a diamond-anvil cell (DAC) [1]. This small mechanical press forces together the tiny, flat tips of two flawless diamond anvils. As the diamond tips slowly compress a microgram sample of a material, where pressure is up to almost 400 GPa. Subsequently techniques in the combination with low temperatures were developed to allow the study of transport properties as well as superconductivity as showed in [2], [3]. This detail will be show in chapter 2.

1.2 Pressure effect on superconductors

High-pressure experiments can provide valuable assistance in the search for superconductors with new value of T_c. The critical temperature of a superconductor depends on both lattice and electronic properties, one in general expects pressure to have a profound and possibly complicated effect on T_c. High pressure studies can advance the field of superconductivity to improve the properties of known superconductors and create new superconductors. McMillan expression [4] is often used for the electron-phonon coupling parameter and equation of the critical temperature for the transition to superconductivity in BCS theory for exploring the effect of pressure on superconductivity.

$$\lambda = \frac{N(E_F) < I^2 >}{M < \omega^2 >} \quad (1) \qquad , \ \eta = N(E_F). < I^2 >$$

$$\Rightarrow T_c \approx \sqrt{k / M}.\exp[-k / \eta] \quad (2)$$

Where $<I^2>$ and $<\varpi^2>$ are the average square electronic matrix element and average square phonon frequency respectively. So that $T_c \propto \sqrt{1/M}$

The spring constant k increases under pressure due to lattice stiffening, and η also normally increases under pressure. The k inside of the exponent in Equation (2) outweighs the k in the prefactor so that an increase in k leads to a decrease in T_c. It is possible for T_c to increase if η increases more rapidly than k under pressure. Therefore, dT_c/dP depends on the relative magnitude of pressure-induced changes in lattice versus electronic properties. In the simple metal superconductors, pressure-induced lattice stiffening dominates over the relatively modest changes in electronic properties so that T_c decreases rapidly under pressure in these materials. In the transition metals, T_c may either increase or decrease under pressure. Fig. 1.1 illustrates pressure effect on simple elements [5].

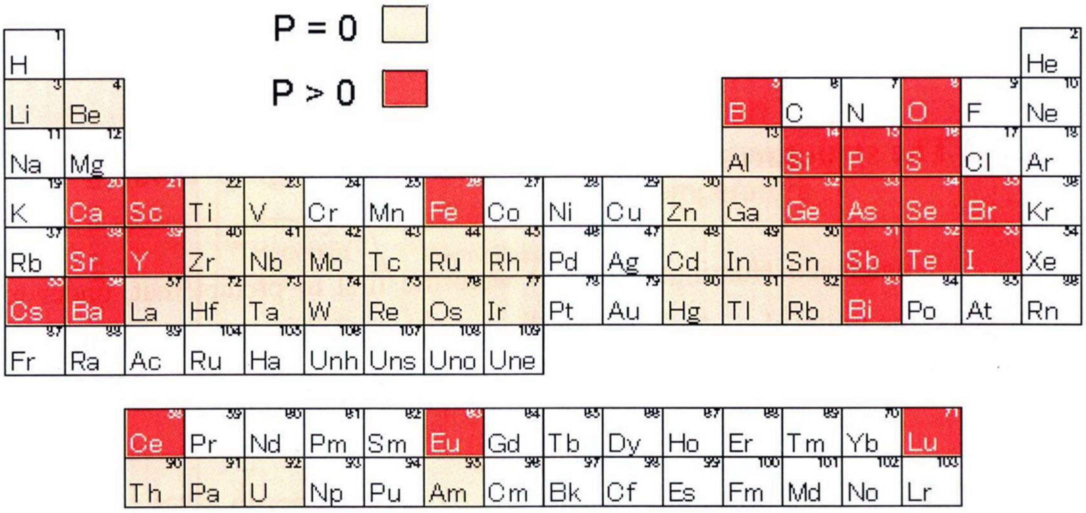

Fig. 1.1: Superconducting elements under high pressure [5]

1.3 High-pressure properties of hydrogen

1.3.1 Hydrogen under high pressure:

Hydrogen is the simplest of all atoms, with a single proton and electron, doubled in the molecule. Hydrogen was first liquefied in 1898 and solidified in 1899 by James Dewar. Both these condensed phases are transparent insulators and had predicted that the condensed phases would be metals at atmospheric pressure. However, the quest for metallic hydrogen has been going on for over one hundred years. At low pressure, hydrogen crystallizes as an insulating molecular solid, but it was recognized that extreme pressure conditions hydrogen would form dense plasma. An idea leading conjecture that all materials will become metallic under sufficiently high pressure. An investigation of the insulator-metal transition in hydrogen have predicted under high pressure. The pressure required to make metallization for hydrogen is so enormous up to 400 GPa [6]. Further predictions for metallic hydrogen may be a room temperature superconductor. This has been directed toward the highest static pressures achieved in DAC with hydrogen remaining an insulating molecular solid by experiment. However, solid metallic hydrogen has not been observed at pressures up to 340 GPa [7], that is about three million times atmospheric pressure and just about the limit of DAC used in such experiments and the required pressure might be as large as 400 GPa.

1.3.2 The structures of solid hydrogen under high pressures

Wigner and Huntington (1935) were the first to predict that, under extreme pressure, the molecules of solid hydrogen will dissociate to form a metallic solid (Fig 1.2), and this was predicted to occur at pressure of 25 GPa [8].

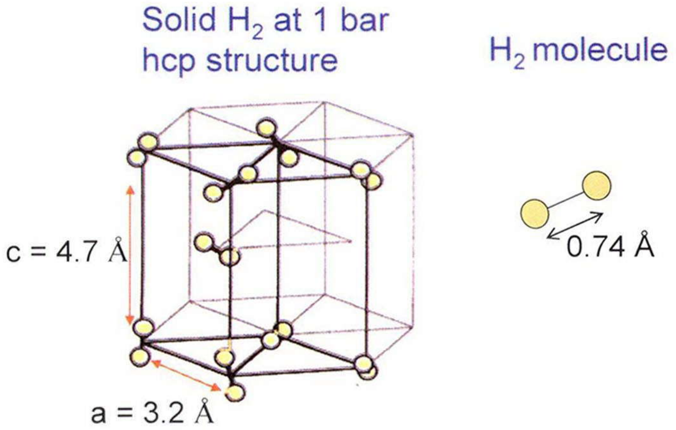

Fig. 1.2: Idealized structures of solid molecular hydrogen (disordered hexagonal-close packed). The bond length in the solid at ambient pressure is that of the free molecule of 0.74 Å and intermolecular distance of 3.2 Å [8].

The crystal structure is one of the most fundamental of information needed for characterizing a material at high pressure. Structural studies of hydrogen at high-pressure in DAC by X-ray diffraction appeared severely restricted by the low intensity of the diffraction peaks. Three different phases, called phase I, II and III, have been experimentally identified through spectroscopic analysis of samples pressurized in DAC as show in Fig. 1.3.

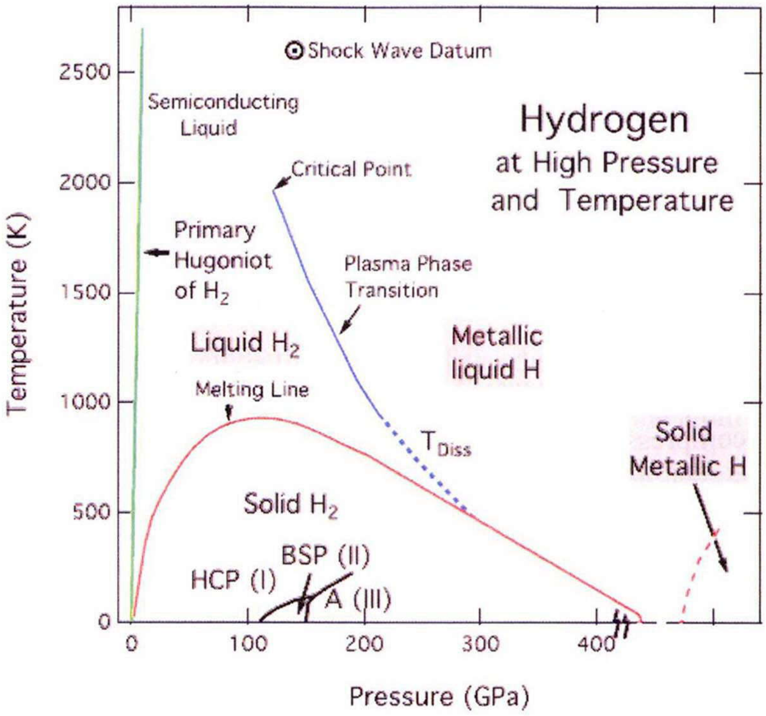

Fig. 1.3: Illustrates the hydrogen phase diagram, summarizing both experimental [9, 10, 11, 12, 13, 14] and computer simulation data [15, 16, 17]

The phase II is stable only in a restricted interval of pressures and for temperatures below 100 K. Phase I occupies the major part of the solid region of the phase diagram, being stable up to the melting in a wide range of pressures. At pressures higher than 160 GPa the phase III appears.

Structural studies of hydrogen solids are not an easy using X-ray diffraction. The electrons of hydrogen atoms are few hence the obtained diffraction patterns are only low resolved. The structures of those phases are not completely determined. Phase I is an hcp, but the molecular rotations are frozen and the molecular bonds are oriented. More recent X-ray and neutron diffraction studies [18, 19] advanced the possibility of the existence of distorted hcp structures for the phase II solid. The structural properties of the phase III are still under debate. According to the analysis of Raman, the most plausible structures for the phase III might be a monoclinic structure belonging to the C2/c space group symmetry for pressures up to 250 GPa [20].

Here some resent topics are shown.

- **Melting curve:** The transition from the low temperature molecular solid to the high temperature molecular fluid phase is well studied experimentally up to 150 GPa [9, 10, 11, 12] as showed in Fig. 1.3. The transition is the shape of the melting temperature curve, which at first increases with the pressure, then reaches a maximum and finally starts to decrease.

- **Metallization in the fluid phase:** A large number of experiments were carried on using dynamic compression techniques in order to study the properties of high-pressure fluid hydrogen [21, 22, 23, 24, 25]. A liquid-liquid transition, from the insulating to the conducting fluid, was observed during shock wave experiments by Nellis. [9]. The insulator-metal transition in hydrogen predictions of the metallization pressure have ranged as high as 200 GPa.

- **Metallization in the solid phase:** Despite the pressures experimentally reached at present are one order of magnitude higher than the Wigner estimated [7] of the metallization pressure (of 25 GPa), no evidence of a metallic behavior has been found in the solid phases, up to 340 GPa [26, 27]. P. Laubeyre reported optical measurements of solid hydrogen up to a pressure of 320 GPa at 100 K. They measure the absorption edge of hydrogen above 300 GPa, observing features characteristic of a direct electronic band-gap. They predict that metal hydrogen should be observed at about 450 GPa when the direct gap closes.

1. 4 Hydride for alternative for dense hydrogen

1.4.1 The hydrogen rich system

Many metals dissolve considerable amounts of hydrogen in an exothermic reaction up to 100 atomic % in transition metals and up to 300 atomic % in rare earth metals. In many compounds the density of the dissolved hydrogen is higher than that of solid hydrogen. We calculated density of hydrogen in the atom unit as show Fig 1.4. Density of hydrogen in YH_3 is 44 atom/nm^3 and solid hydrogen is 37 atom/nm^3. There showed that YH_3 is more the dense of hydrogen than hydrogen solid.

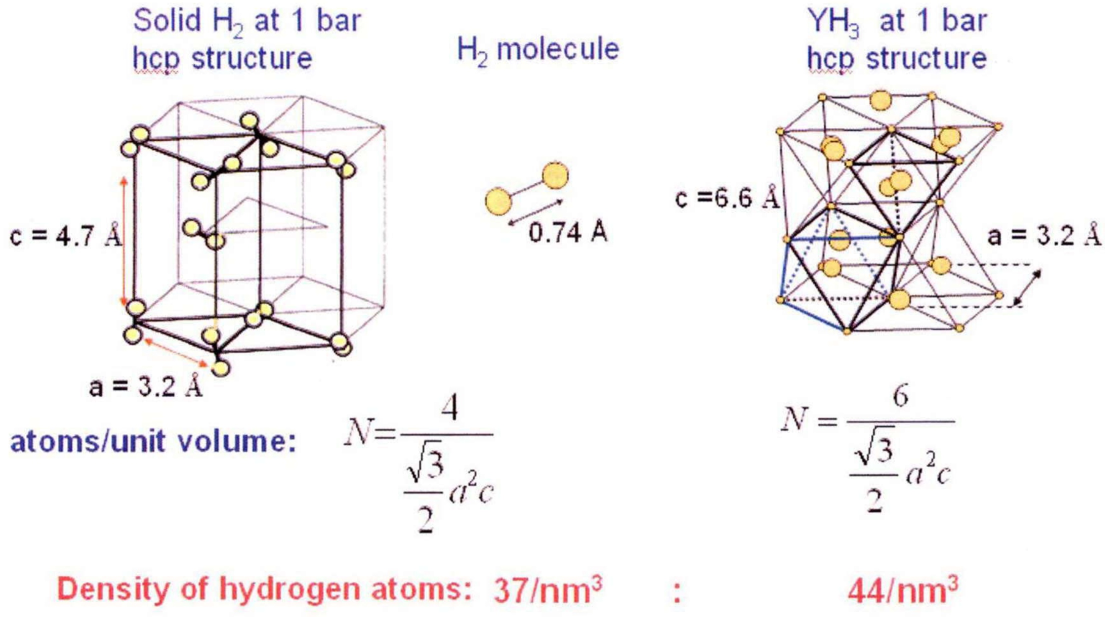

Fig. 1.4: Compounds the density of the dissolved hydrogen is higher than that of solid hydrogen

1.4.2 Chemical pre-compression in hydride

The pressurized hydrogen-rich materials are expected as alternative approach which may offer a great promise that could a so-called “chemical pre-compression” from the metal atoms combines and additional pressure facilitate hydrogen densities in the range where the metallization could occur. For example, metallization in silane

(SiH_4) has been experimentally observed [28, 29] and was analyzed from a theoretical perspective [30]. Much metal hydride- MH_3 system with M(Y, Sc, Er, Lu, Al, ...)- investigated for metallization and superconductivity.

1.4.3 Hydrogen dissociation and hydride formation

Far away from the surface, the H_2–molecule and the metal are in their respective ground states. The hydrogen molecule dissociates and absorb into Y pure metal lattice as show in Fig 1.4 [31]. Close to the metallic surface *van der Waals* forces between the molecule and the metal surface result in a physisorbed state.

In the reference [31], they showed that the H–M bond was of electronic nature, on the surface as well as in the bulk. Whenever the hydrogen atom approaches the metal, its 1 *s* electron hybridizes with the electrons of the metal. The resulting hydrides can be classified by the nature of the hydrogen bond into three different principal categories, covalent, ionic or metallic. The term "hydride" will be used to describe the binary combination of hydrogen and a metal.

- *Covalent hydrides* may be solid, liquid or gaseous. The H–M bond is of the non–polar electron sharing type. Forces between the molecules of covalent bonded hydrides are not strong, resulting in low melting points. Most of them are thermally unstable. Typical examples of covalent hydrides are aluminum hydride, tin hydride and the boron hydrides.

- *Ionic hydrides* are formed by the reaction of the strongly electropositive metals like alkali metals and hydrogen by electron transfer. Their bonds result from the strong electrostatic forces between the dissimilar electric charges of the ions. The saline hydrides are crystalline. They exhibit large heats of formation and high melting points.

- *Metallic hydrides* are formed by the transition metals. They possess metallic properties like thermal conductivity or hardness. Because of the wide homogeneity ranges of most of the metallic hydrides, they are often regarded as solid solutions. There are two models describing the chemical bond of metallic hydrides. In this model, Yttrium forms metallic hydrides. The H–Y system will be discussed in detail in the chapter 3.

1.4.4 Predicted T_c of YH_3 under high pressure

Pure yttrium becomes superconducting under pressure and the T_c increases monotonically with pressure up to 115 GPa (with $T_c = 19.5$ K) [32]. Few theoretical calculations using linear response theory [35, 36] to estimate T_c have found qualitative agreement with the experiment [32] as shown Fig 1.5.

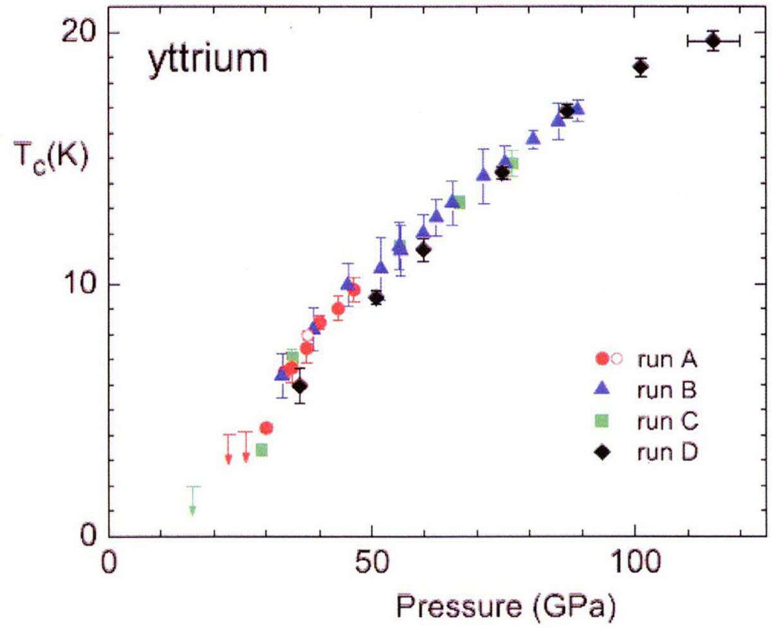

Fig. 1.5: Superconductivity transition temperature T_c of fcc Y with pressure.

Yttrium can form a hydride able to absorb about 300 mol% hydrogen, which is a yellowish transparent insulator with hcp-structured YH_3 at ambient pressure [38]. In experiment, hcp-YH_3 transforms sluggishly into fcc-YH_3 near 10 GPa [33, 37] and becomes a metal at around 25 GPa [33]. Therefore, in theory, there is the possibility to study high- T_c superconductivity in hydrogen-dense materials with fcc-YH_3 under pressure [39].

Fig. 1.6a displays a schematic of the fcc-YH_3 crystal structure at 17.7 GPa combined with the electron localization function. There exist one type of yttrium atom occupying the fcc site and two types of hydrogen: H(1) and H(2), tetrahedral and octahedral coordinated, respectively. In Fig. 1.6(b–e), there have the shift of peak at three pressure values (15, 30, and 45 GPa) near Fermi level. At lower pressure, the electron belonging to H(2) is responsible for a peak near the Fermi level (Fig. 1.6, b–e), strongly affecting conductance properties of YH_3. With increasing pressure, this peak shifts towards higher energy values, leading to a reduction in conductivity. . Based on first-principles calculations as discuss in [39], assessing the electron-phonon coupling strength λ , there predict high-temperature superconductivity in fcc-YH_3.

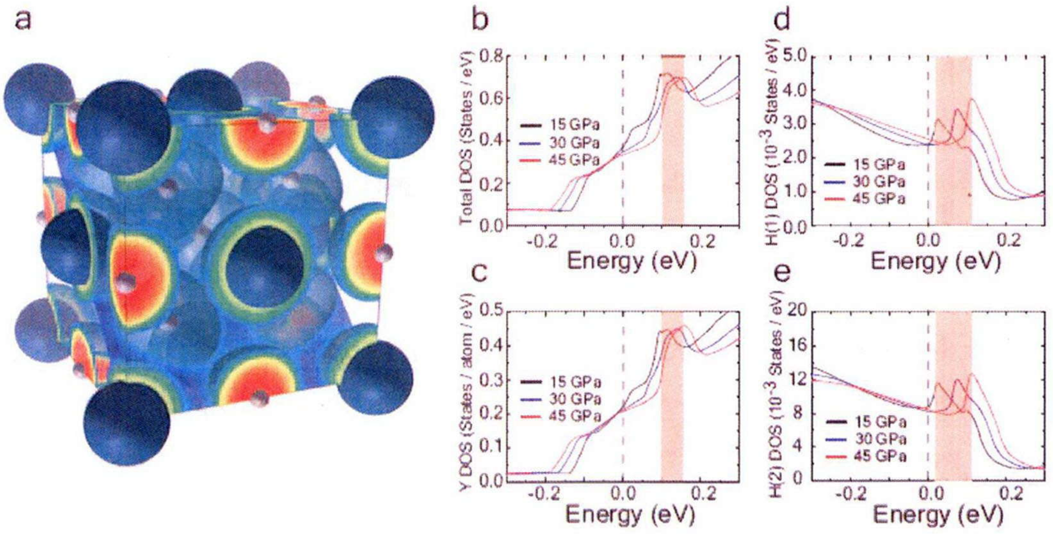

Fig. 1.6: Electronic structure of cubic YH_3. (a) Crystal structure and electron localization function plot at 17.7 GPa. Blue spheres represent yttrium, while white small spheres represent hydrogen, with H(1) at tetragonal sites and H(2) at octahedral sites. Electron density of states plot in fcc-YH3. (b) Total DOS and projected DOS onto (c) Y, (d) H(1), and (e) H(2) near E_F for three different pressure values. The vertical dashed line indicates the position of the Fermi level and the shaded regions exhibit the peak-shift with pressure [39].

As it can be seen in Fig. 1.7a, the occurrence of pressure-induced superconductivity with T_c of 40 K at 17.7 GPa in the high-pressure fcc phase of YH_3 based on calculations of D.Y. Kim [39], and T_c will be decrease at higher-pressure value. From Fig. 1.7a, it finds a steep drop in T_c at a pressure of around 25 GPa, which is a transition from superconducting to normal metallic state. Upon higher pressure, where is expressed the superconducting behavior above 45 GPa, and fcc-YH_3 remains in the metallic state until 45 GPa. So that, there is showed the pressure-dependence of T_c in fcc-YH_3.

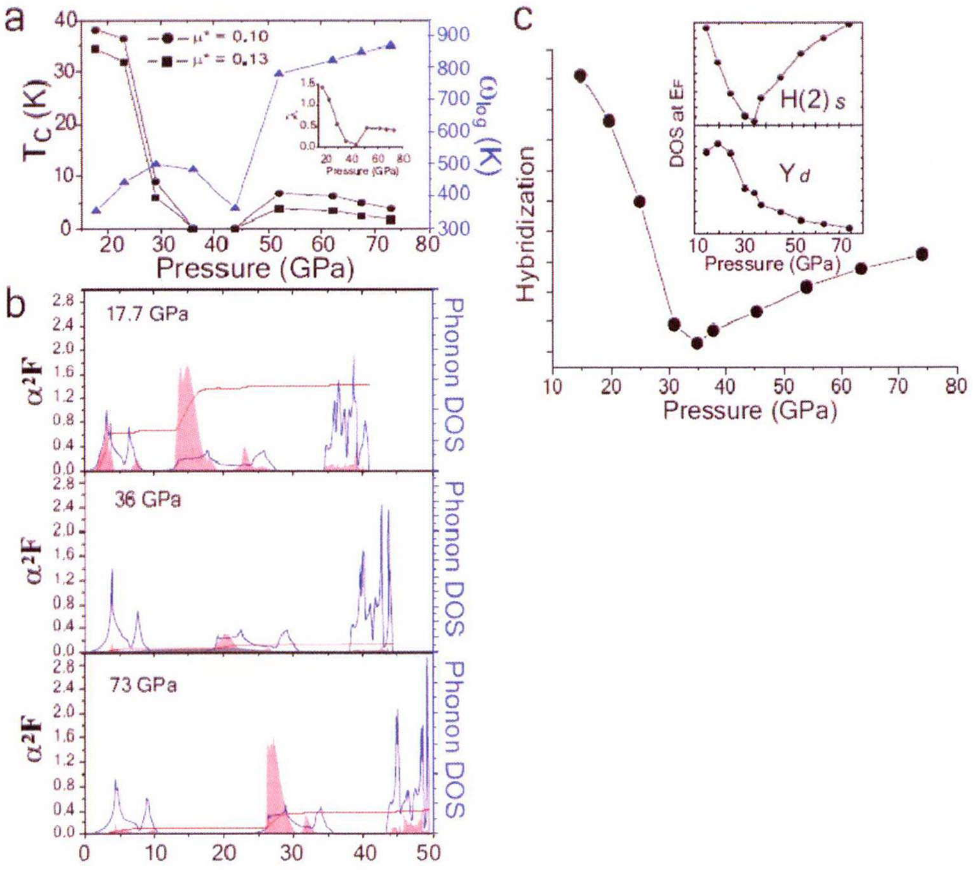

Fig. 1.7: (a) Pressure dependency of T_c and ω*log*. The inset shows the evolution of the electron-phonon coupling constant λ with pressure. (b) shows the spectral function α2*F* (red shaded area), integrated λ (red line), and phonon DOS (blue curves) as a function of frequency at *P* = 17.7, 36, and 73 GPa, respectively. (c) Hybridization between *d*-state of Y (lower panel of the inset) and *s*-state of H(2) (upper panel of the inset) at the Fermi level under pressure.

References

[1] K. Shimizu et al., *J. Phys. Soc. Jpn.* 74, 1345 (2005).

[2] A. Jayarama, *Review of modern Phys.*, Vol.55, No.1 Jan 1983.

[3] M. Eremets, High pressure experimental methods, 1996 (Book)

[4] W. L. McMillan, *Phys. Rev.*, 167(2):331–344, 1968

[5] J. Hamlin, PhD thesis 2007, Washington univ.

[6] P. Loubeyre, F. Occelli and R. LeToullec, *Nature* 416, 613 (2002)

[7] E. Wigner and H. B. Hungtington, *J. Chem. Phys.* 3, 764 (1935)

[8] H. K. Mao and R. J. Hemley, *Rev. Mod. Phys.* 66, 671 (1994)

[9] S. T. Weir, A. C. Mitchell and W. J. Nellis, *Phys. Rev. Lett.* 76, 1860 (1996)

[10] M. I. Eremets and I. A. Trojan, *JETP letters* 89, 174 (2009)

[11] F. Datchi, P. Loubeyre and R. LeToullec, *Phys. Rev. B* 61, 6535 (2000)

[12] S. Deemyad and I. F. Silvera, *Phys. Rev. Lett.* 100, 155701 (2008)

[13] E. Gregoryantz, A. F. Goncharov, K. Matsuishi, H. K. Mao and R. J. Hemley, *Phys. Rev. Lett.* 90, 175701 (2003)

[14] I. I. Mazin, R. J. Hemley, A. F. Goncharov, M. Hanfland, and H. K. Mao, *Phys. Rev. Lett.* 78, 1066 (1997).

[15] S. A. Bonev, E. Schwegler, T. Ogitsu and G. Galli, *Nature* 431, 669 (2004)

[16] S. Scandolo, *PNAS* 100, 3051 (2003)

[17] M. Morales, et al., *PNAS* 107, 12799 (2010)

[18] P. Tolédano, et al., *Phys. Rev. Lett.*103, 105301 (2009)

[19] I. Goncharenko and P. Loubeyre, *Nature* 435, 1206 (2005)

[20] M. Hanfland, R. J. Hemley, and H. K. Mao, *Phys. Rev. Lett.* 70, 3760 (1993)

[21] W. J. Nellis, et al., *J. Chem. Phys.* 79, 1480 (1983)

[22] G. W. Collins, et al., *Phys. Plasmas* 5, 1864 (1998)

[23] D. G. Hicks, et al., *Phys. Rev. B* 79, 014112 (2009)

[24] M.D. Knudson, et al., *Phys. Rev. B* 69, 144209 (2004)

[25] G.V. Boriskov, et al., *Phys. Rev. B* 71, 092104 (2005)

[26] C. Narayana, H. Luo, J.Orloff and A. L. Luoff, *Nature* 393, 46(1998)

[27] P. Loubeyre et al. Nature, 383, 702, 1996

[28] X. J. Chen, et al. Proc Natl Acad Sci USA, 105:20–23. (2008).

[29] M.I. Eremets, Science, 319:1506–1509. (2008)

[30] D. Y. Kim DY, et al. Proc Natl Acad Sci USA, 105:16454–16459. (2008)

[31] R. Griessen , Review Optical properties of metal-hydrides: switchable mirrors June 2005

[32] J. J. Hamlin, *et al.,* Phys. Rev. B, 73 (9): 094522, 2006.

[33] W. L. Johnson, in R. Beck and A. J. Guntherod (eds.), Glassy Metals I, Top. Appl.

[34] R. Griessen, *Europhysics News* (2001) Vol. 32 No. 2

[35] S. Lei, *et a, Phys. Rev*. B, 75 (2): 024512, 2007

[36] Z. P. Yin, *et al., Phys. Rev. B*, 74 (9): 094519, 2006

[37] T. Kume, *et al., Phys. Rev*. B, 76 (2): 024107, 2007.

[38] J. N. Huiberts *et al., Nature*, 380 (1996) 231

[39] D. Y. Kim *et al., Phys. Rev. Lett.*, 103 (2009) 077002

[40] M. I. Eremets and I. A. Trojan, *JETP letters* 89, 174 (2009)

Chapter 2. Experimental

In this session, the use of the diamond anvil cell (DAC) for ultrahigh-pressure generation and the various techniques employs in studying under high pressure are mainly reviewed. There are descriptions of technique for measurements of the electrical resistance at low temperatures, x-ray diffraction and so on.

2.1 Diamond-Anvil Cell (DAC)

The DAC is very simple and is illustrated in Fig. 2.1. The main body of the cell was made of a Cu-Be alloy to make good thermal conductivity. A pair of diamond anvils is set in opposed anvil configuration. When a metal gasket is compressed between the small flat faces of two diamonds, high pressure is generated in the gasket hole, which is usually filled with a pressure transmitting medium, or the sample itself. The cell works at high pressure, when the two anvil flats are accurately centered and parallel to each other. The selection of diamond type and the culet size are needed to employ the maximum pressure [1].

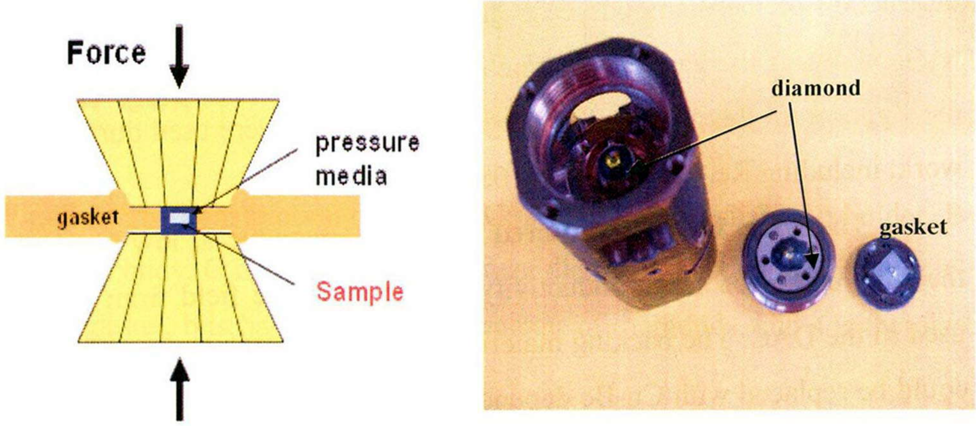

Fig. 2.1: The DAC is based upon the opposed-diamond configuration, in which a sample is placed between the polished culets of two diamonds and is contained on the sides by a metal gasket (left). Main body of the DAC was made of a Cu-Be, non-magnetic material (right).

Following properties can be studied with DAC:

- Crystal structure by diffraction of X-rays or neutrons
- Electrical resistivity
- Optical properties, such as absorption, reflection, and luminescence

The top of anvil can be repolished, it is possible some shallow cracks or damage appears after experiment. Parallelism of the culet flat with the diamond table is important. That is the most dangerous points at top of the anvils. The anvils need a large force, and high pressure can occur to plastic deformation of the seats and possible failure of the anvil.

A key component of the diamond anvil cell is the gasket. The gasket reduces the strain at the diamond culets and makes it possible to surround the sample with a pressure medium. The gasket foil is first pre-indented to a thickness dependent on the diameter of the diamond culet. The pre-indented thickness should be approximately 1/9 of the culet diameter and 1/3 of the hole diameter. The hole is drilled through the center of the pre-indented area. The purpose of gasket is to provide a chamber in which can be contained a sample with pressure medium. Depending on the sample and pressure medium, the initial diameter of the hole should be adjusted the diameter of hole at high pressure. The gasket material must be both hard and ductile. If the gasket's ductility is too low, it can suffer brittle failure under pressure, resulting in destruction of the diamonds. The gasket material must remain non-magnetic at low temperature. If the gasket is magnetic, the signal from the sample will be obscure by the signal from the gasket. Several gasket materials were used during this dissertation work, including Re, Cu-Be, SUS310S....

The DAC was also required to be non-magnetic at low temperature to avoid the suppression of superconductivity by the magnetic field from the magnetic parts used in the DAC. The backing material was made of WC (tungsten-carbide)-alloy and could be replaced with Cu-Be depending on the experiment. The high-pressure device is the screw pressure-type DAC, as schematically shown in Fig. 2.3. A is the upper diamond holder, B is the main body, C is the piston with lower diamond, D is the driving nut, G is metal gasket, b is ball bearing, d is the pair of diamonds, and s is the plastic ring. The cell body of our DAC is made of nonmagnetic Be–Cu alloy favorable for characterization of magnetic properties of sample. The generation of pressure is usually carried out at room temperature, but different thermal contraction of each component gives rise to unexpected increment in pressure upon decreasing the temperature and results in change of pressure. To avoid the big change of pressure at low temperature, a plastic ring (s) is inserted between the driving nut (D) and piston (C) inside the DAC. The large thermal contraction of the plastic ring provides considerable compensation for the pressure difference. The pressure is generated by pushing the piston (C) to advance into the cell body (B) through rotating the driving nut (D) with the blade of gearbox mechanism. Two ends of a screw bolt can fit into the screw groove machined on the piston and sliding tube, respectively.

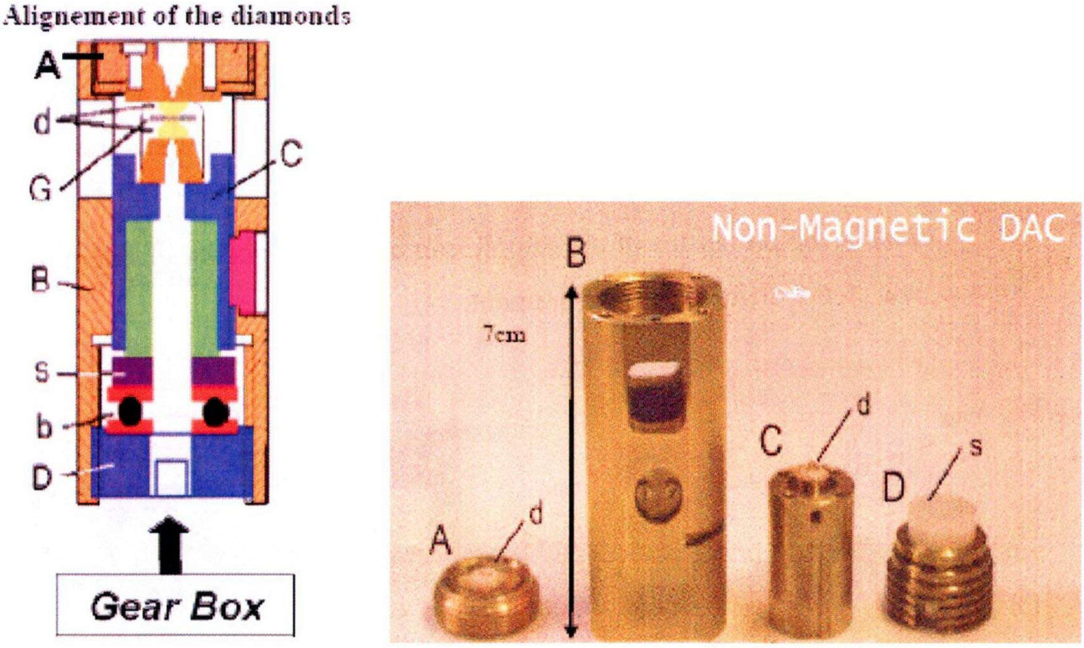

Fig. 2.3: The construction of the DAC: A is the upper diamond holder, B is the main body, C is the piston with lower diamond, D is the driving nut, G is metal gasket, b is ball bearing, d is the pair of diamonds, and s is the plastic

2.1.1 Sample setting

Fig. 2.3 shows our typical experimental setup in this study.

- First a metal gasket is compressed between two small flat surfaces (flattened by grinding and polishing of the culet) of two diamonds set in opposed anvil configuration. For the successful operation of the diamond cell, the two anvil flats should be accurately centered ad set parallel to each other. After that, and sample hole is made using laser cutting technique. After the hole is made, sample can be prepared by the desired shape and dimension in Fig. 2.4a.

- The next step is sample setting inside the DAC, involving putting pressure medium, putting the sample inside the hole, connecting the electrodes to the sample, and putting ruby as pressure reference. In this experiment, these samples are highly reactive with water, oxygen and nitrogen. To avoid the chemical reaction and contamination of the sample, it was kept inside a glove box filled with Ar-gas in Fig. 2.4b. All procedures of the sample preparation and pressure cell loading were carried out inside the glove box. After loading sample, the pressure was increased to some pressure to seal the sample chamber completely. Pressure inside the diamond anvil cell is adjusted by pressure gearbox and pressure measurement is done using ruby fluorescence method.

- Finally, the properties of the sample can be determined by electrical resistivity, Raman, and X-ray diffraction measurement.

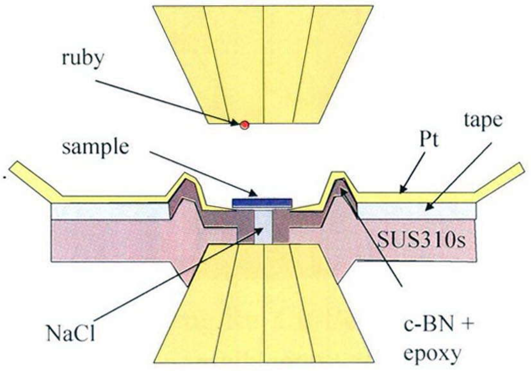

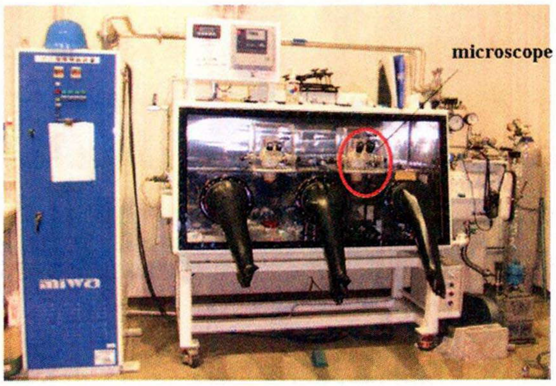

Fig. 2.4a. DAC: The culet of the diamond anvil: 300 μm; gasket material: SUS310S; thickness of gasket: 50μ m; insulator layer: diamond powder +epoxy; electrode material: Pt; pressure media : NaCl

Fig. 2.4b: Inside the glove-box is full of Ar-gas and O_2, H_2O level $\leq$ 1 ppm (0.001%)

2.1.2 Pressure determination

Pressure was determined by the conventional ruby fluorescence. Ruby has a strong luminescent doublet at 694.2 nm (R1) and 692.8 nm (R2) at room temperature, which comes from the transition between the crystal electric fields levels. Ruby can be efficiently pumped into an excited state by illumination with light. The shift in the R1 line is used to determine pressure as shown in Fig. 2.5.

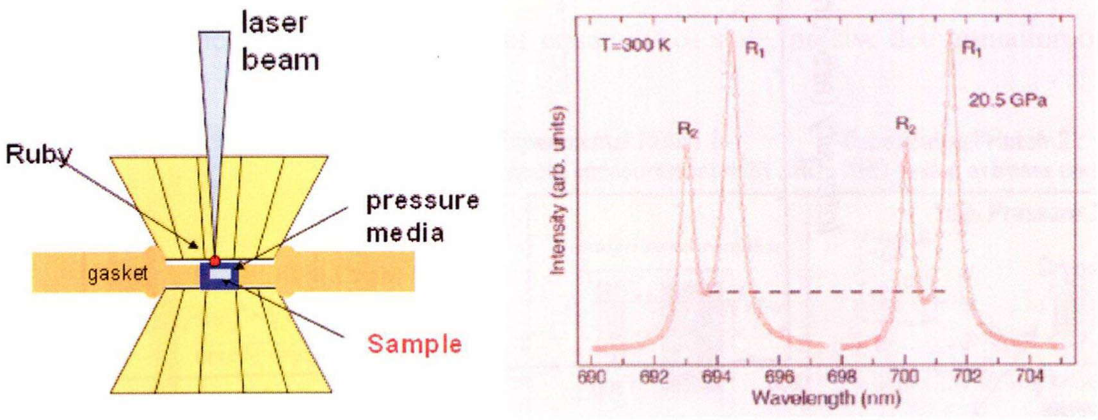

Fig 2.5. The Ruby luminescence line at GPa pressure and atmospheres pressure [8]. The fluorescence lines show red-shift with pressure. The shift in the R1 line is used to determine pressure (right).

When the pressure is applied up to around 100 GPa the intensity of the R1-line decreases. So that pressure was determined by the first-order Raman band spectra of the diamond anvil facing to the sample. The high frequency edge was defined as a minimum of the differential spectrum, dI / $d\upsilon$, as shown in the Fig. 2.6. The high frequency edge of the Raman band shows the nearly linear pressure dependence [2, 3]. The dependence is almost independent on loading conditions Since the diamond vibron shifts monotonically to higher frequency under pressure, the high-frequency edge of the anvils Raman spectrum gives the pressure at the center of the culet where the sample is located. The most recent calibration of the high-frequency edge of the Raman spectrum of the diamond anvil is that of Akahama et al. [9]. Using the equation of state of platinum as a standard and found that the calibration is nearly independent of the gasket material, sample or pressure medium. Pressure is expressed by the following quadratic function of the Raman frequency υ (cm^{-1}).

$$P(GPa) = 66.9(7) + 0.5281(4) \text{ x } \upsilon + 3.585(3) \text{ x } 10^{4} \text{ x } \upsilon^{2}$$

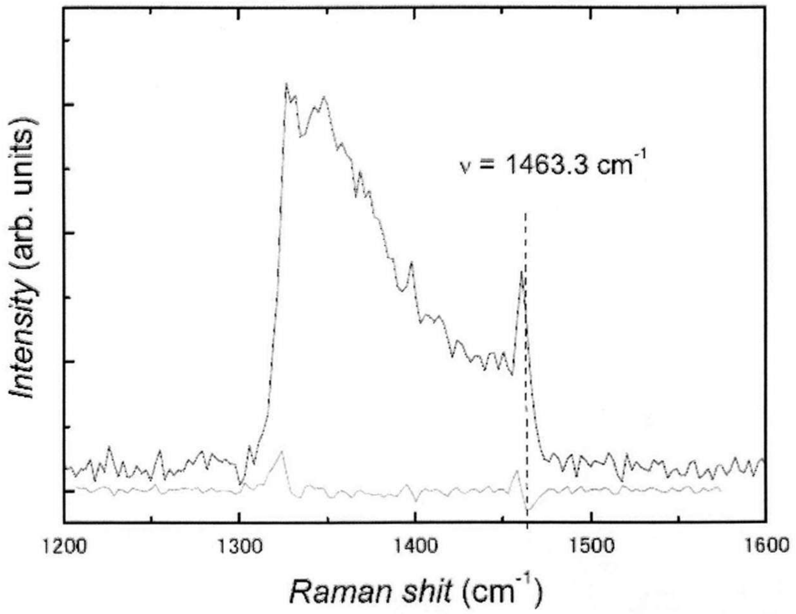

Fig. 2.6: Raman band was determined from differential spectrum *dI* / *d*υ, indicated with a gray line [8].

This may be particularly useful in the case of optical absorption measurements where having ruby within the cell may falsify the results since some of the light will pass through the ruby pieces instead of the sample. In addition, the diamond vibron manometer is useful in the case of studies (such as resistivity), which often use no pressure medium; in this situation large pressure differences may exist between the sample and ruby if they are not directly on top of each other. With the diamond vibron of the anvil, one can always measure the pressure at the same lateral location as the sample.

2.2 Measurements

2.2.1 X-ray diffraction

Crystal structure at high pressure is studied using X-ray diffraction. We performed X-ray diffraction measurement on materials at the pressures at room temperature using synchrotron radiation with wavelength of around 0.41 Å at the beamline BL10XU in the SPring-8.

The beamline BL10XU is fully dedicated for X-ray diffraction measurements at high pressure and low/high temperature using a diamond anvil cell (DAC) (Figure 2.7) [5]. The high-resolution monochromatic angle-dispersive X-ray diffraction patterns allow us to the accurate determination of equations of state, precise determination of

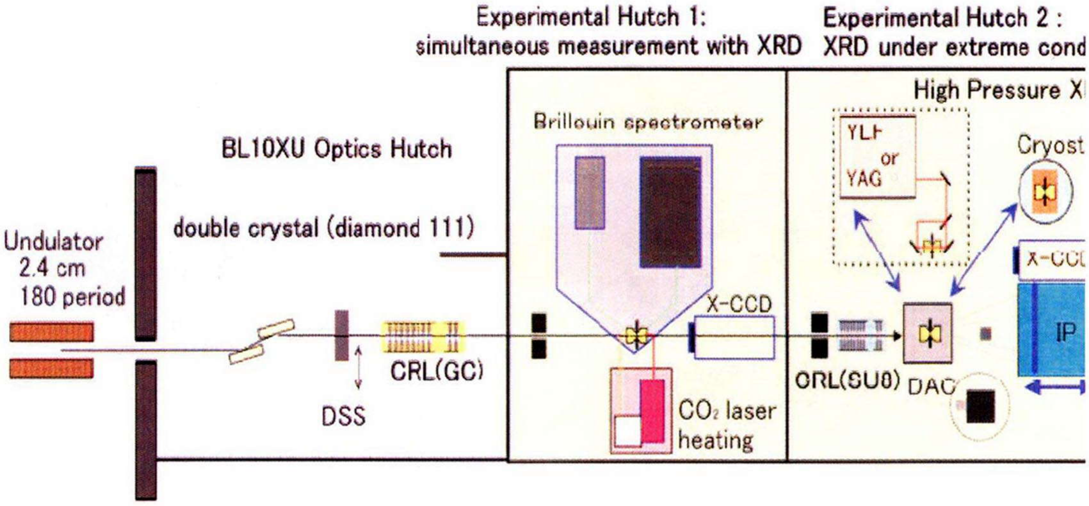

Figure 2.7. Schematic layout of beamline BL10XU [5]. The DAC was placed in the Hutch 1 or Hutch 2. X-ray is focused an collimated to approximately a few μm in FWHM using polymer refractive lenses (SU-8). The collimated X-ray passes through the optical windows and the sample in a DAC with the cell axis oriented along the X-ray beam. Diffracted X-ray was collected on a imaging plate (IP). Conventional diffraction diagrams were obtained by integration of the two-dimensional images using PIP software. The X-ray wave length was varied 0.4102 Å(30 keV) and 0.4976 Å(25 keV).

phase relation, structure refinement by Rietveld analysis, and charge density distribution analysis in crystals submitted to extreme pressures.

2.2.2 Electrical resistance measurement

The technique for resistivity measurements in DAC was performed with ac four-probe method. Four Pt films with 5 μm in thickness were attached to the sample. The metal gasket is pre-indented and coated with an insulating mixture of cubic boron nitride (c-BN) powder and stycast epoxy. The insulation between the electrodes can hold up even under extreme pressure. A sample chamber can be drilled into the insulating material by focused laser beam.

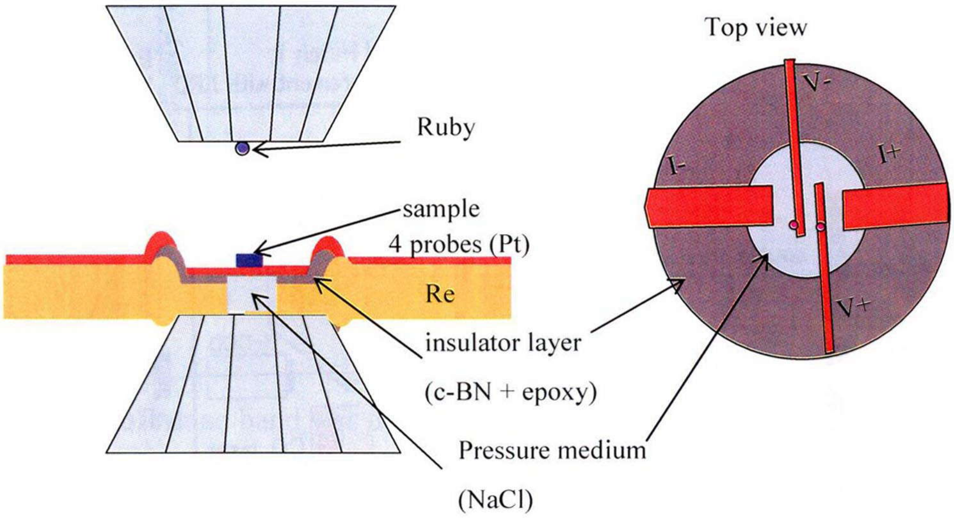

Fig. 2.8 The electrical resistivity was measured by ac 4-probes. Arrangement of sample and electrodes in the DAC: Ruby for pressure marker; sample; Pt film electrode (5 μm^t); insulator layer; pressure medium (NaCl); metal gasket (Re).

Electrodes with sharp tips are cut from 5-μm thick platinum foil. The wires contacted to the sample by pressing the wires against the sample in the diamond anvil. The configuration around sample is shown in Figs. 2.8.

2.2.3 Low temperature measurement

The majority of superconducting transitions measured at low temperature. The temperature range can close to the 50 mK. For electrical measurements at low temperature, we used a Top-loading ^{3}He/^{4}He dilution refrigerator down to ~50 m K. In Fig. 2.9, the most parts of the DAC are consisted of the non-magnetic Cu-Be alloy to

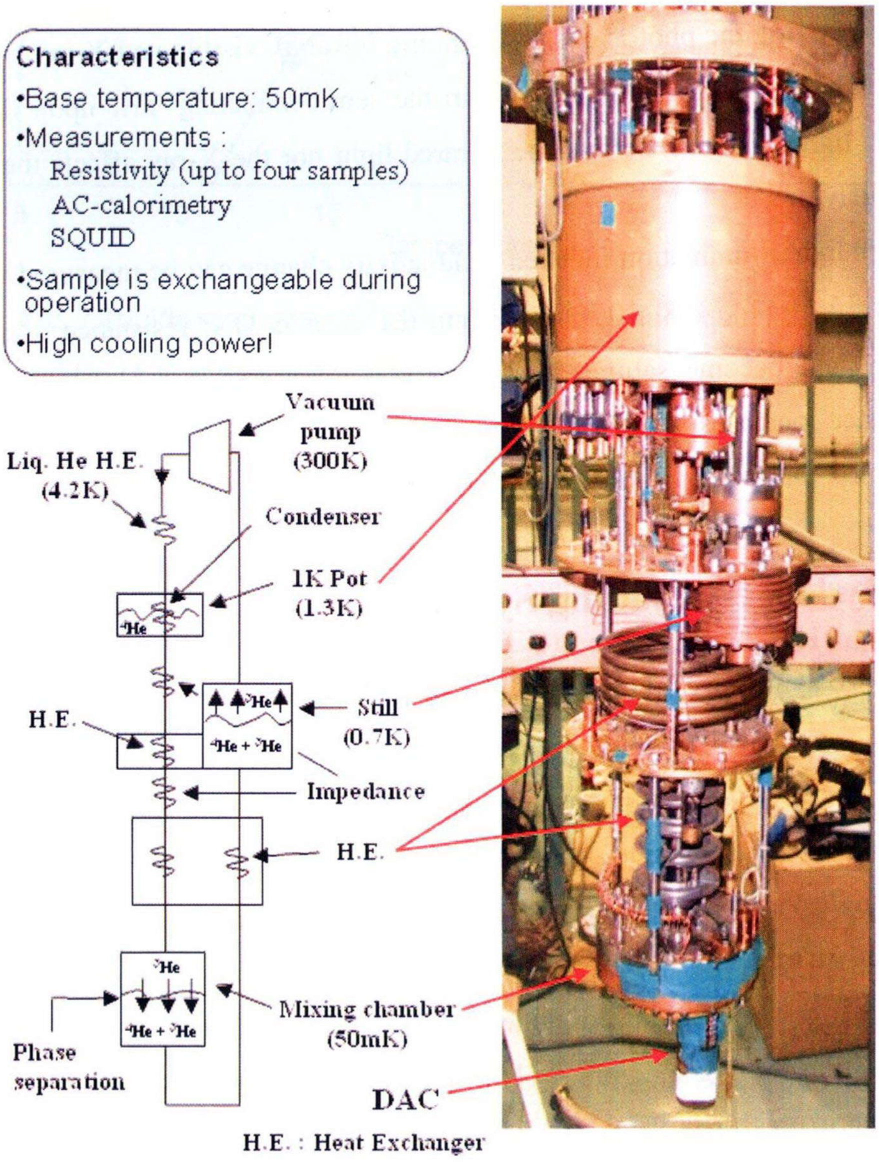

Characteristics
- Base temperature: 50mK
- Measurements :
  - Resistivity (up to four samples)
  - AC-calorimetry
  - SQUID
- Sample is exchangeable during operation
- High cooling power!

Fig. 2.9: The electrical resistivity measurements were carried out in a ^{3}He/^{4}He dilution. Lowest temperature: 50 mK; measurement of resistivity up to 3 samples.

make thermal conductivity good. Temperatures were determined below 5 K using the calibrated RuO_2 resistance thermometer, and the CERNOX resistance thermometer was used above 5 K. We usually and clamped the pressure at room temperature before low-temperature runs. The DAC was fixed on the mixing chamber of the $^3He/^4He$ dilution refrigerator. The detail is showed in reference [4].

2.2.4 Photoconductivity via visible light at high pressure

By varying the photon energy spanning infrared, visible and X-ray, we manifested significantly enhanced conductivity in the semiconducting YH_x upon illuminated by visible light, whereas, neither the infrared light nor the X-ray affects the conductivity obviously.

The light illumination-induced conductivity change can be measured with different light of λ = 514, 488, 1064 nm. Upon the laser is ON, resistance of sample drops rapidly and become saturated within 10 minutes. Once the laser is switched off, resistance increases gradually and eventually resumes the initial value within a large relaxation time. The detail will be study in chapter 3.

2.3 Hydrogen Loading System

To synthesize YH_3, we developed the loading the gas in cryostat system. With a simple method the diamond anvil cell (DAC) is cooled at low temperature in the region of liquid phase diagram of gases and the gas flowed into chamber as a liquid. The samples were prepared from the yttrium metal.

The simplest method to load the DAC with hydrogen is to place in a vessel [7]. Thermodynamic equilibrium parameters of the solid-liquid-gas phase transition (Fig. 2.10) are very important to understand the process. Hydrogen also works as a pressure-transmitting medium. Hydrogen was liquid at 20 K, and solid < 15 K at atmospheric pressure.

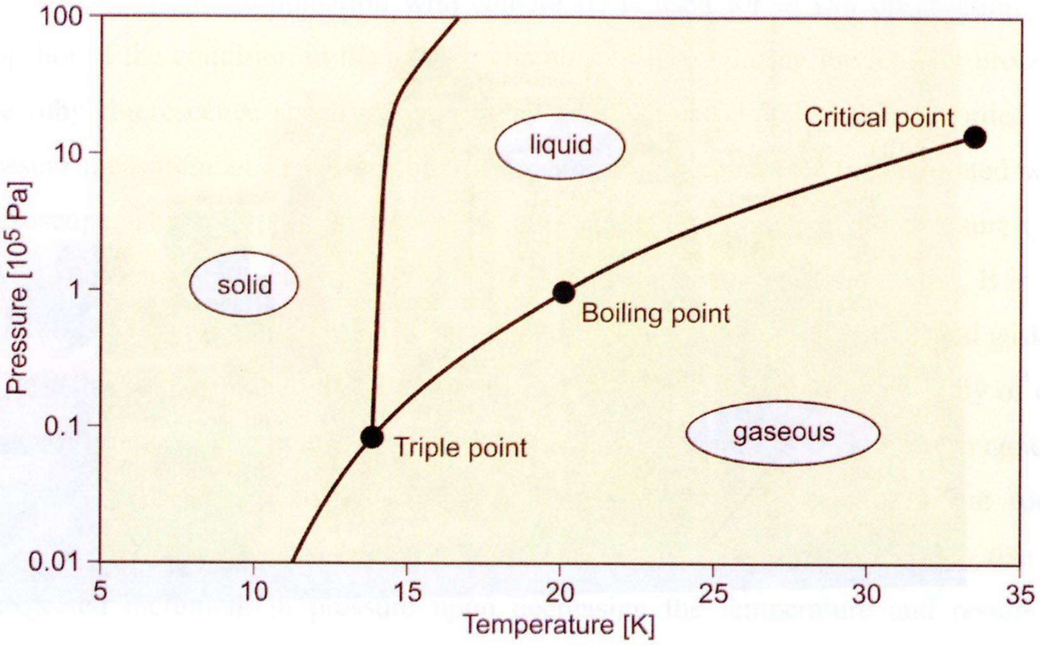

Fig. 2.10: Phase diagram of hydrogen. Hydrogen is liquid at 20 K, and solid < 15 K at atmospheric pressure.

2.3.1 Instrumentation

As shown in Fig. 2.11(a), the whole system consists of packaged vacuum pumping unit (DS-A312Z, DIAVAC LIMITED), cryostat, gearbox mechanism, helium compressor unit (CKW-21, Sumitomo Heavy Industries, Ltd.), cold head (RDK-205D, Sumitomo Heavy Industries, Ltd.), microscope (Lambda Vision), spectrometer (Ocean Optics), temperature controller (32B, CRYOGENIC CONTROL SYSTEMS, Inc.) and computer. The schematic diagram of the whole system and the portion highlighting the DAC and the "sliding tube" in the liquid H_2 reservoir is displayed in Fig. 2.11(b) and Fig. 2.11(c), respectively. The packaged pumping unit (e) evacuates the liquid H_2 reservoir (o) and outer vacuum chamber of the cryostat (m) for thermal insulation with ambience. The helium compressor unit (l) runs to refrigerate the cold head in a closed cycle mode. The thermal link (n) between cold head and liquid reservoir is realized with bundles of copper wire. One window (p) is made on the side of cryostat to observe the liquid level in the reservoir; the other window (p) made on the bottom of cryostat is used for observation of the sample assembly.

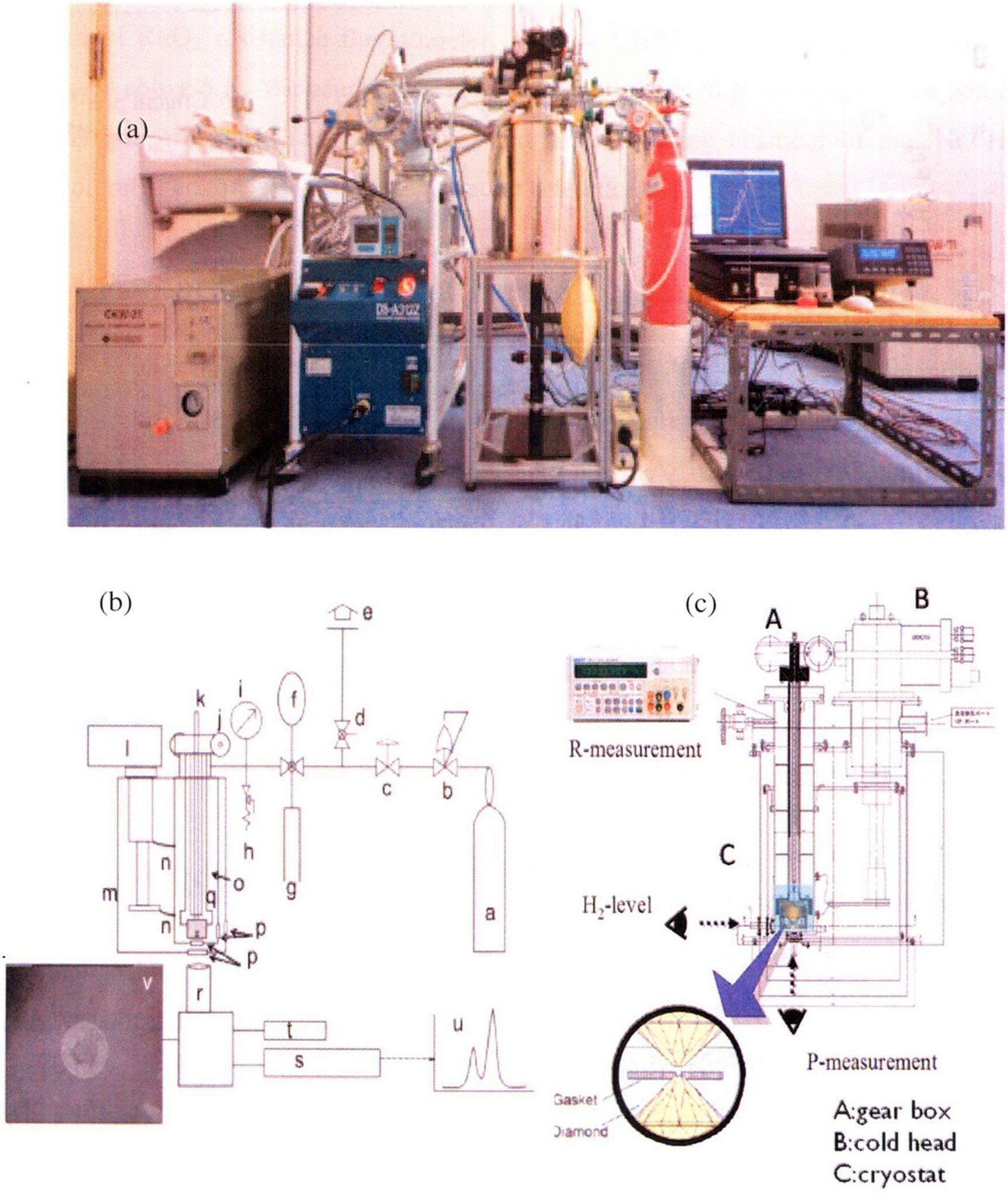

Fig. 2.11: (a) Photograph of the cryogenic loading system;
(b) Schematic diagram of the whole system; a: H_2 gas bottle, b: regulator, c: gasflow control valve, d: valve, e: packaged vacuum pump, f: a balloon which is used to count introduced gas amount, g: exhaust tube for excessive H_2 gas, h: relief valve, i: pressure gauge, j: gearbox system, k: sliding tube, l: closed cycle refrigerator, m: cryostat, n: bundles of metal wires, o: liquid H_2 reservoir, p: optical windows, q: DAC holder, r: microscope and camera system, s: spectrometer, t: laser, u: ruby fluorescence output, v: photo image outputted on a monitor, w: inner tube, x: DAC body, y: DAC piston, and z: driving nut.

Microscope in combination with camera (r) is used for *in situ* observation and snapshot of the condition in the sample chamber of DAC during the loading process. The ruby fluorescence spectrum excited by green laser (λ=532 nm) is recorded for pressure measurement in the sample chamber using spectrometer (s) integrated with microscope. The high-pressure device we commonly adopt is the screw pressure-type DAC, as schematically shown in Fig. 2.12(a). A is the upper diamond holder, B is the main body, C is the piston with lower diamond, D is the driving nut, G is metal gasket, b is ball bearing, d is the pair of diamonds, s is the plastic ring. The cell body of our DAC is made of nonmagnetic Be-Cu alloy favorable for characterization of magnetic properties of sample. The generation of pressure is usually carried out at room temperature, but different thermal contraction of each component gives rise to unexpected increment in pressure upon decreasing the temperature and results in breakage of diamond. To avoid the failure of diamond at low temperature, a plastic ring (s) is inserted between the driving nut (D) and piston (C) inside the DAC. The large thermal contraction of the plastic ring provides considerable compensation for the pressure difference. Sample chamber made by laser ablation in the center of pre-indented metal gasket is used for containment of sample, pressure marker and pressure medium. The pressure is generated by pushing the piston (C) to advance into the cell body (B) through rotating the driving nut (D) with the blade of gearbox mechanism. Two ends of a screw bolt can fit into the screw groove machined on the piston and sliding tube, respectively. Optical fiber transmitting backlight for better visualization of the sample assembly during loading process is inserted in the hole of screw bolt and extends to the exit port on top of the gearbox mechanism. Fig. 2.12(b) is the photograph of the gearbox mechanism. The blade for rotating the driving nut of DAC and the screw bolt for opening the sample chamber are highlighted. Fig. 2.12(c) is the photograph of DAC clamped with jacket. Fig. 2.12(d) is the photograph of DAC assembled with gearbox mechanism. The gearbox mechanism (j) is equipped with two inner tubes. One inner tube (w) with larger diameter is assembled with a blade which can rotate the driving nut of DAC to control the force applied to the piston, hence control the pressure in the sample chamber. The other inner tube with smaller diameter, named "sliding tube" (k), passing through the center of the larger inner tube, is assembled with a screw bolt which can fit into the screw groove machined on the

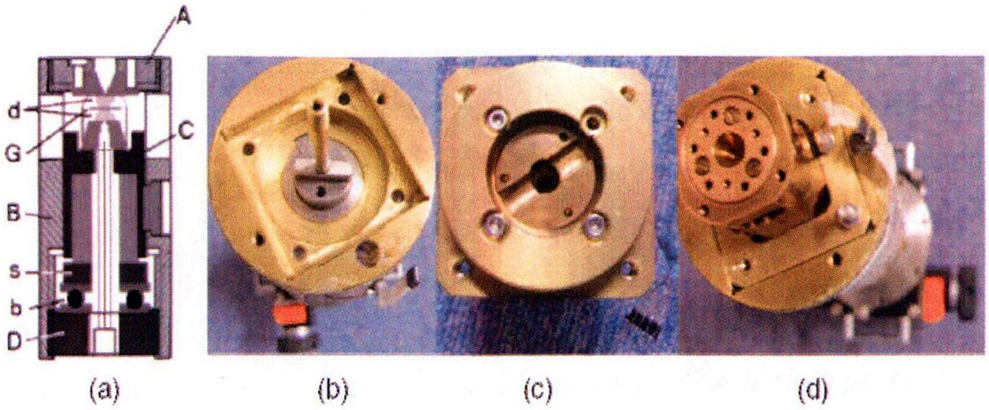

Fig. 2.12: (a) Schematic diagram of the screw-pressure type DAC; (b) Gearbox mechanism; (c) DAC with clamping jacket; (d) DAC installed in the holder of gearbox mechanism

piston of DAC. Using this "sliding tube", the operator can control the gap between the culet of diamond anvil and gasket by moving the piston from outside the cryostat, hence, the sample chamber of DAC can be opened and closed freely.

As a result, start over of the loading is enabled. Additionally, the "sliding tube" mechanism can circumvent the contamination of sample by opening the sample chamber after the surrounding atmosphere is evacuated and replaced by H_2 or D_2 in the liquid reservoir, which is crucial for alkali metal, alkaline-earth metal, and rare-earth metal, because they are chemically reactive with oxygen, water, and even nitrogen. The combination of camera, spectrometer and microscope considerably enhances the success rate and ensures the desired initial pressure for different loading.

2.3.2 Procedure of loading gases

At first, In the middle of the culet of one diamond, a foil yttrium is cut with a thickness around 1μm and loaded into the sample chamber. To avoid the chemical reaction and contamination of the sample, Y was kept inside a glove box filled with Ar-gas. All procedures of the sample preparation and pressure cell loading were carried out inside the glove box and transferred into the cryostat, as shown in Figure 2.13a [7]. The status of the sample and pressure marker assembly in the sample chamber is monitored by the microscope camera. The laser beam for exciting the ruby fluorescence spectrum transmitted in optical fiber is focused on the ruby chip in the sample chamber for pressure measurement. After the liquid reservoir is pumped to be free of air and moisture, the sample chamber of DAC is opened by the "sliding tube", as shown in Fig. 2.13b One balloon of H_2 gas is introduced into the liquid reservoir as cryogen. Afterwards, the closed cycle refrigerator is switched on to cool down the cryostat. The temperature of DAC is controlled to be stable between the melting point and boiling point of H_2 by temperature controller. H_2 gas counted by balloon is introduced into the liquid reservoir until the liquid level is above the surface of sample chamber, as shown in Fig. 2.13c. The wavelength of the ruby fluorescence R1 line is measured as reference for further pressure measurement upon trapping the liquid in the sample chamber. The liquid is captured in the sample chamber by squeezing at desired initial pressure, as shown in Fig. 2.13d. The sample is gradually hydrogenated by stepwise warming up to room temperature, as shown in Fig. 2.13e. Therefore, the pressure was applied to 3 GPa and kept constant with the gearbox system during warming up to room temperature. Finally, Yttrium was kept surrounded by H_2 liquid in DAC at 3 GPa at room temperature.

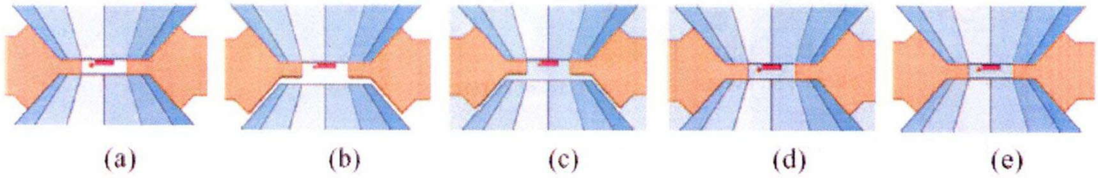

Fig. 2.13 Schematic illustration of the loading process. (a) The DAC is installed into the liquid reservoir. (b) The sample chamber is opened and the DAC is cooled down to below the boiling point of H_2 gas. (c) The liquid level is increased to above the sample chamber. (d) The liquid is sealed in the sample chamber. (e) The DAC is warmed up to room temperature.

2.3.3 Sample preparation of YH_3

Figure 2.14 shows our typical experimental setup in this study. In this experiment, the YH_3 sample is made by loading H_2 liquid with Y metal in low temperature. Therefore the sample yttrium hydride surrounded with hydrogen liquid was prepared in DAC with the a sample hole drilled on a gasket. Hydrogenation results the yellow-transparent YH_3 phase in shown Fig. 3.15.

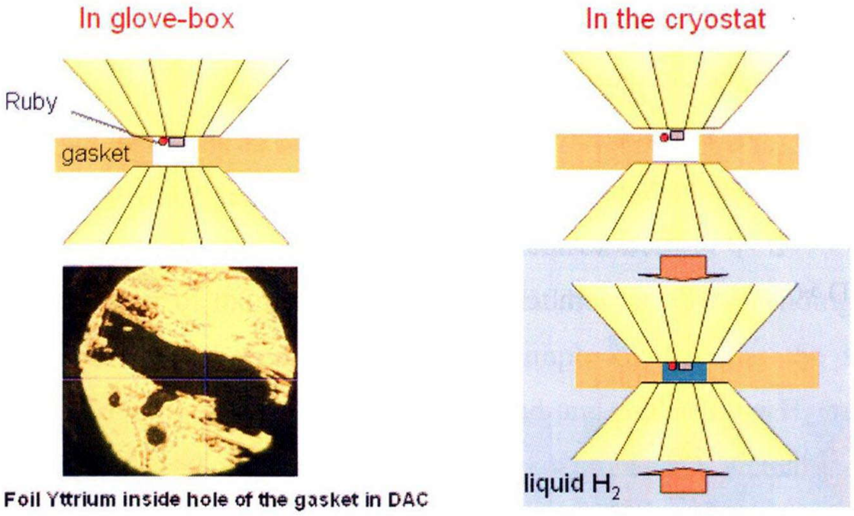

Fig. 2.14: YH_3 sample is made by loading H_2 liquid with Y metal in low temperature. The yttrium sample was placed into a DAC with the sample hole drilled in a gasket. Ruby powder as pressure marker was compacted with the sample. The sample was loaded in an argon-gas grove box (left). The sample in DAC was then cooled down to liquid hydrogen temperature and the hydrogen gas was flowed into the chamber in the cryostat. Y was kept surrounded by H_2 liquid in DAC at 3 GPa and warmed up to room temperature (right).

We performed resistance measurements with ac four-probe with 4 Pt wire attach to the sample in a chamber made by an electrical insulator with cBN-NaCl mixture. Ruby chip as pressure marker were compacted in the sample chamber such as shown in Fig. 2.16.

The synthesized YH_3 sample was transformed from the first DAC to the second DAC and attached to the measurement probes. Pressure was applied at room temperature and a $^3He/^4He$ dilution refrigerator was used for low temperature measurement.

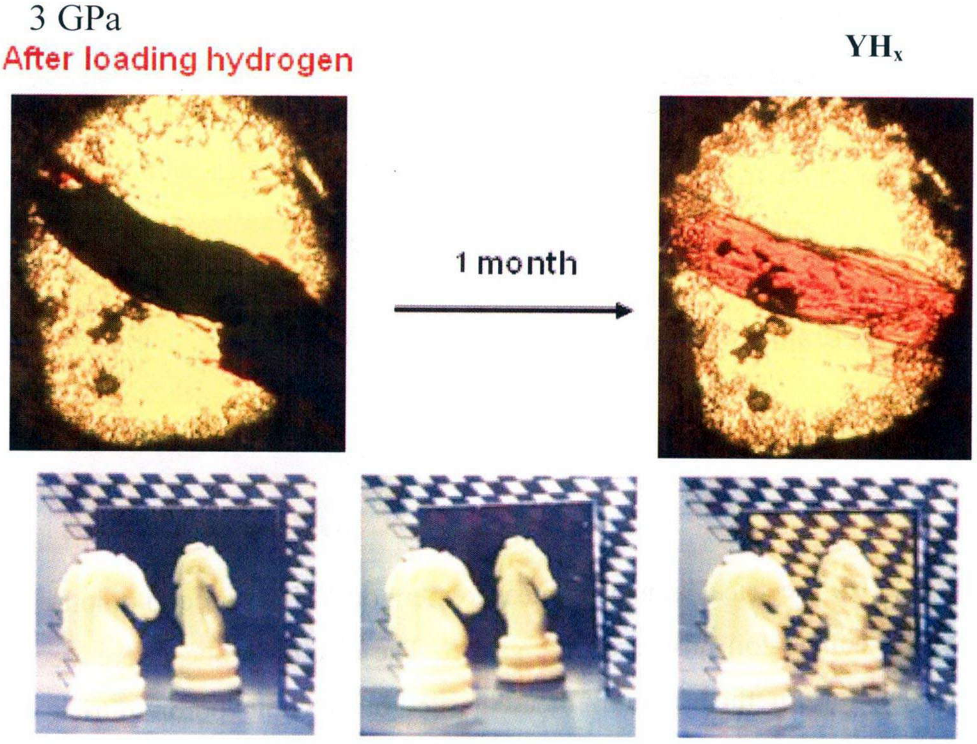

Fig. 2.15: Hydrogenation in liquid H_2 at room temperature. Hydrogenation results in the yellow-transparent YH_3. The result showed the same transparent film with Huiberts group [10]. To make sure hydrogenation, we wait enough time, here take 1 month for hydrogenation.

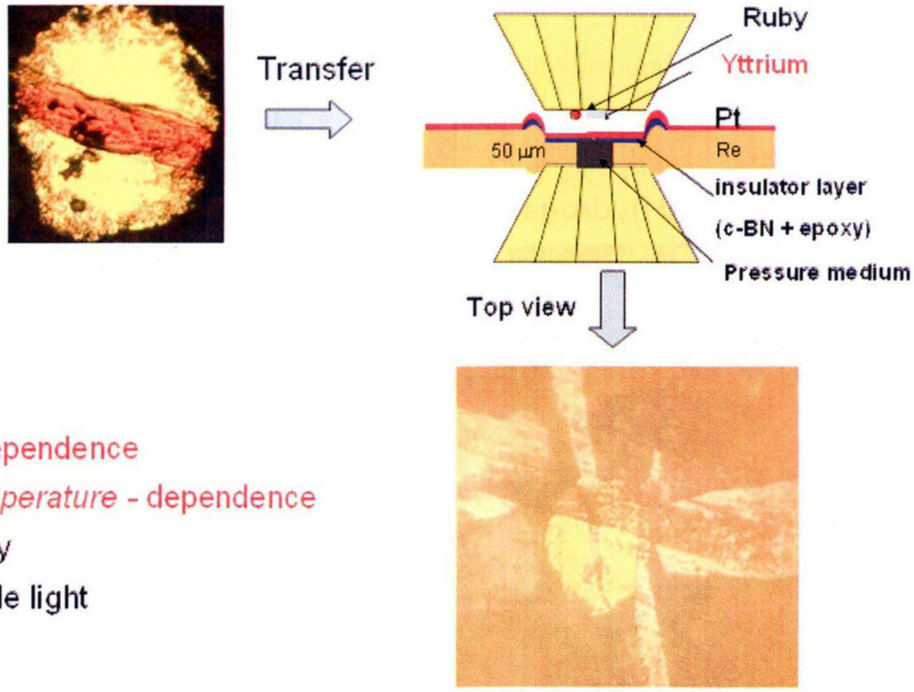

Fig. 2.16: Electrical resistance measurement on YH_3. A second (another) DAC with 4 copper-foil probes on the gasket. The electric probes were electrically insulated from the rhenium metal gasket by a cubic boron nitride (c-BN) powder. Ruby powder as pressure marker was compacted with the sample. The synthesized YH_3 sample was transformed from the first DAC to the second DAC and attached to the measurement probes.

References

[1] A. Jayaraman, Review of Modern Physics, Vol.55, No.1, January 1983

[2] Y. Akahamaa and H. Kawamura, J. Appl. Phys. 96, 3748 (2004).

[3] M. Hanfland and K. Syassen, J. Appl. Phys. 57, 2752 (1985).

[4] K. Shimizu *et al.*, Proceeding of AIRAPT-17, Hawaii, 1999, p.77.

[5] Y. Ohishi *et al.*, *High Press. Res.* 28, 163 (2008).

[6] A. Ohmura *et al.*, Appl. Phys. Lett. 91 (2007) 151904

[7] Z. Chi *et al.*, Rev. Sci. Instrum. 82, 105109 (2011)

[8] T. Matsuoka, doctor thesis 2008, Marie-Aude Méasson, *NG-SCES – June 2010.*

[9] Y. Akahama and H. Kawamura, J. Appl. Phys., 100:043516, 2006.

[10] J. N. Huiberts *et al.*, Nature, 380 (1996) 231

Chapter 3. High-pressure effect on yttrium hydride

Huiberts et al. [1] discovered that thin films of $YH_{3-\sigma}$ can be switched between a reflecting mirror and a transparent insulator by varying their hydrogen content, and this has generated a great amount of attention over the past years. At ambient conditions, it was found by neutron-diffraction measurements that the fully hydrogenated state (YH_3) crystallizes in hexagonal structure. At high pressure, YH_3 undergoes a structural phase transformation induced and that this transformation is accompanied by a metal-insulator transition [2-6]. Recently, a theoretical prediction indicated the occurrence of pressure-induced superconductivity with T_c of 40 K at 17.7 GPa in the high-pressure fcc phase of stoichiometric YH_3 [7]. In this chapter, synthesized sample by hydrogenation from pure yttrium was pressurized in a diamond-anvil cell and the pressure-dependent and temperature-dependent resistance measurements were carried out. We found that the insulator-metal transition is driven by the considerable negative slope of $d\rho/dT$.

3.1 Properties at ambient pressure

Hydrogen in metals has been investigated since Graham discovered in 1866 that palladium can absorb large amounts of hydrogen gas. Apart from Pd, there are numerous other metals which exhibit the ability to absorb hydrogen. Within the metal, the H_2 molecule is dissociated and the H atoms occupy interstitial sites in the host lattice.

The process of hydride formation can be explained as in reference [8]. The H-M bond is electronic nature. Whenever the hydrogen atom approached the metal, its 1 s electron hybridizes with the electrons of the metal. New bonding and antibonding bands will form within the metal. The resulting hydrides can be classified by the nature of the hydrogen bond into three different principal categories, covalent, ionic or metallic.

The interaction of H_2 with metal leads to absorption and the formation hydrides which depends on the thermodynamic conditions. In the case of yttrium hydride, the phase diagram consists of three basic parts as shown in Fig. 3.1 [1].

- α phase: metallic solid solution of hydrogen in yttrium (hcp).

- β phase: metallic dihydride (fcc) with two H atoms situated in two available tetrahedral sites of the metal lattice.

- γ phase: Trihydride (hcp) with a bigger unit cell than the original metal, and filling up both tetrahedral sites and one octahedral site.

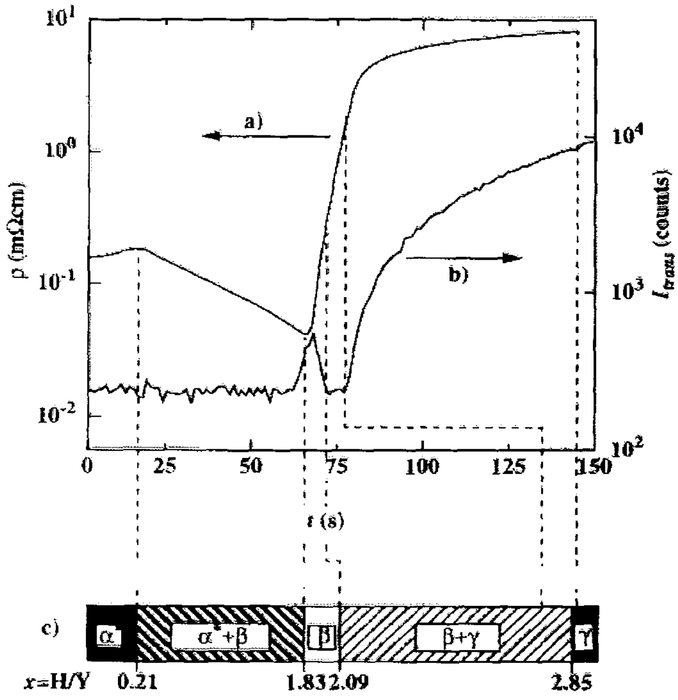

Fig. 3.1: Electrical resistance (a) and optical transmission for 1.8 eV photons (b) during hydrogen [1].

3.1.1 Electronic properties

The increase in ρ with increasing H concentration in Fig.3.1 is indications of the occurrence of a metal-insulator (MI) transition. ρ increases with increasing hydrogen concentration up to the α phase limit, but the sample remains shiny metallic [10]. When the Y is hydrogenated up to the β–phase, the two H–atoms per unit cell add two extra electrons to the system. For Y, the value of the resistance decreases to 20% in the dihydride phase. YH_2 is a better metal than pure Y. The main reason for the increased electrical conductivity is the reduced electron phonon coupling. ρ increases with increasing the hydrogen content above the limit of the β–phase, leads to a growing volume fraction of the hexagonal γ–phase. YH_3 becomes insulator by hydrogenation via an increase of the resistance of several orders of magnitude.

3.1.2 Optical switching

In 1995, Huiberts [1] discovered that yttrium and lanthanum hydride show spectacular reversible optical changes when loaded from the dihydride to the trihydride phase. Thin film samples are extremely reactive with oxygen. However, Huiberts prepared thin films of yttrium by evaporation under UHV conditions. Before exposure to air they are covered by a thin layer of Pd to prevent the yttrium from oxidation and at the same time to catalyze the hydrogen absorption [1]. In Fig. 3.2, these photographs show the behavior of a 50 nm thick Y film covered with a 20 nm palladium protection layer in black part. The chessboard pattern is behind yttrium film.

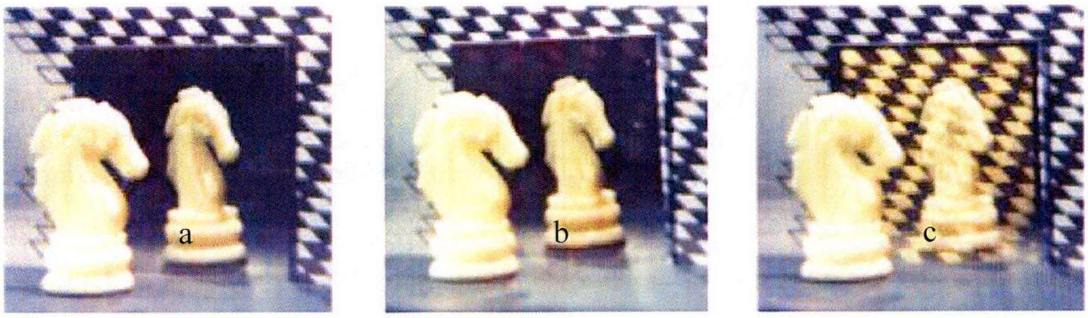

Fig. 3.2: Hydrogenation results in the yellow-transparent [16]. The left picture is yttrium film (a). Upon hydrogen absorption, the film is transformed into the fcc YH_2 phase, which has a weak transmission as shown in the middle picture (b). Further hydrogenation results in the yellow-transparent hcp YH_3 phase at the right side (c).

Chess is in front of the film to see the mirror image. Before hydrogenation, Y film is metal and virtually all the photons in the visible range are reflected. The mirror image of the knight is clearly visible (a). Upon hydrogen absorption, the film is transformed into the fcc YH_2 phase, which has a weak transmission as shown in the middle picture (b). Further hydrogenation results in the yellow-transparent hcp YH_3 phase at the right side (c) which is insulator with band gap ~ 2.8 eV.

3.1.3 Crystal structure

There is an important problem to determine the roles interstitial hydrogen (H) atoms play in structural and electronic properties. Y metal is one of special interest because of their ability to absorb up to three hydrogen atoms per metal atom. Yttrium has the hcp $P6_3/mmc$ structure at room temperature [11] with lattice constants a = 3.3648 Å and c = 5.732 Å. Within this structure the metal atoms occupy places with atom co-ordinates at (0, 0, 0) and (1/3, 2/3, 1/2). Tetrahedral interstitial sites (T–sites) are located at (0, 0, 1/4-z), (0, 0, 3/4+z), (1/3, 2/3, 1/4+z), and (1/3, 2/3, 3/4-z) with z = -1/3(c/a)2. Octahedral interstitial sites (O–sites) occur at (1/3, 2/3, 1/4) and at (2/3, 1/3, 3/4).

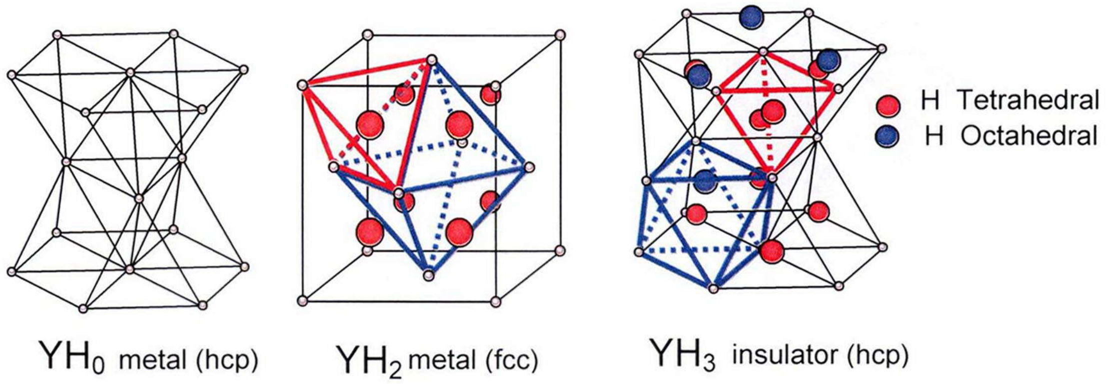

Fig. 3.3: Hydrogen position under ambient pressure [16].

YH_2: two H atoms situated in two available tetrahedral sites of the metal lattice with an fcc structure phase.

YH_3: hydrogen is filling up both tetrahedral sites and one octahedral site with a structural change from cubic to hexagonal.

Yttrium trihydride, YH_3, exhibits a hexagonal metal lattice, which contains three H atoms per metal atom in the interstitial spaces under ambient conditions in Fig. 3.3. Two H atoms are located at the tetrahedral (T) sites and the remaining H atom is located near the Y metal plane in the octahedral (O) sites. On the other hand, dihydride YH_2 has an fcc metal lattice in which the T sites are filled with H atoms. YH_x exhibits a gradual opening of the band gap during hydrogenation over $x = 2$ with a structural change from cubic to hexagonal. Hexagonal YH_3 eventually becomes transparent at a gap of 2.8 eV. Upon dehydrogenation into YH_2, insulating YH_3 transforms into metallic YH_2 with a reversible hexagonal-cubic structural transition. It is considered that the interstitial H atoms, especially the O-site H atoms, play a dominant role in the hydrogen induced band-gap opening as well as in the structural transition.

3.2 Previous works

3.2.1 Metallic behavior under high pressure

. The phase stability of YH_3 under high pressure was studied in the framework of density function theory [14]. The crystal phase stability is analyzed by evaluating the enthalpy ($H = E+PV$). Figure 3.4 shows the calculated enthalpy difference as a function of pressure for the hexagonal and cubic phases of YH_3. The calculations correctly describe the ground state of YH_3 and find that the hexagonal phase is energetically more favorable near the equilibrium volume. However, under compression the hexagonal YH_3 undergoes a structural phase transformation and the cubic phase becomes energetically more stable. Thus the metallic state has been observed in this pressure region around 25 GPa, in agreement with experimental findings showing that the metallic fcc phase appears above 25 GPa [3,6].

The effect of pressure on the electronic properties of cubic YH_3 is investigated through the band structure. In Fig. 3.5, the valence band is mostly due to the hybridization between Y d and H s states whereas the conduction band is primarily formed by Y d states. Clearly, the Fermi level lies in the conduction band giving rise to a metallic state. The GW corrected band overlap at the Γ point is 0.38 eV. However, if the 4p states of Y are taken into account in the calculations as semicore states, the overlap is reduced to 0.15 eV whereas if 4s and 4p states are included as semicore states, the overlap is further reduced to 0.12 eV.

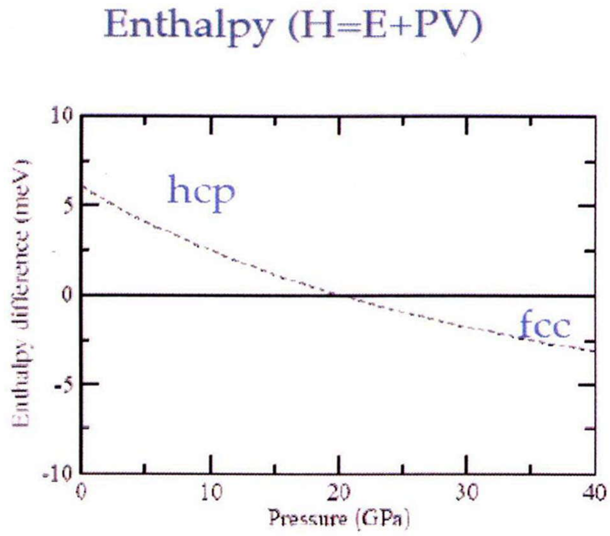

Fig. 3.4: Enthalpy difference as a function of pressure for YH_3 [14].

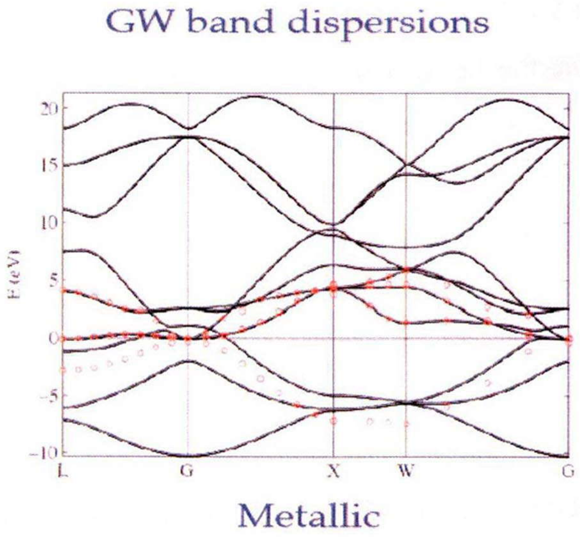

Fig. 3.5: Electronic band structure along with the GW corrections for the cubic phase of YH_3 [14].

3.2.2 Structural phase transition

Ahuja *et al.* predicted that YH_3 undergoes a structural phase transformation induced by pressure and that this transformation is accompanied by a metal-insulator transition [2]. According to the density functional calculation of Kelly [12], a transition from an insulating distorted to metallic phase is expected at 15% decrease of the molar volume, corresponding to 14 GPa applied pressure. Using high-pressure experiment, the pressure-induced structural transition has been investigated using synchrotron radiation X-ray diffraction measurement at room temperature [3,4,5,13]. The hexagonal-fcc transition starts around 11 GPa and is complete near 20 GPa in Fig 3.5 [13].

Machida *et al.* [5] performed X-ray diffraction studies on YH_3. The diffraction patterns do not show apparent changes up to 10 GPa. As pressure increases beyond 11 GPa, the reflection peaks from the hexagonal structure gradually loose intensity and several new peaks appear. A simple diffraction pattern with five reflection peaks is obtained at pressures above 20 GPa and the observed reflection peaks are completely indexed with a fcc unit cell.

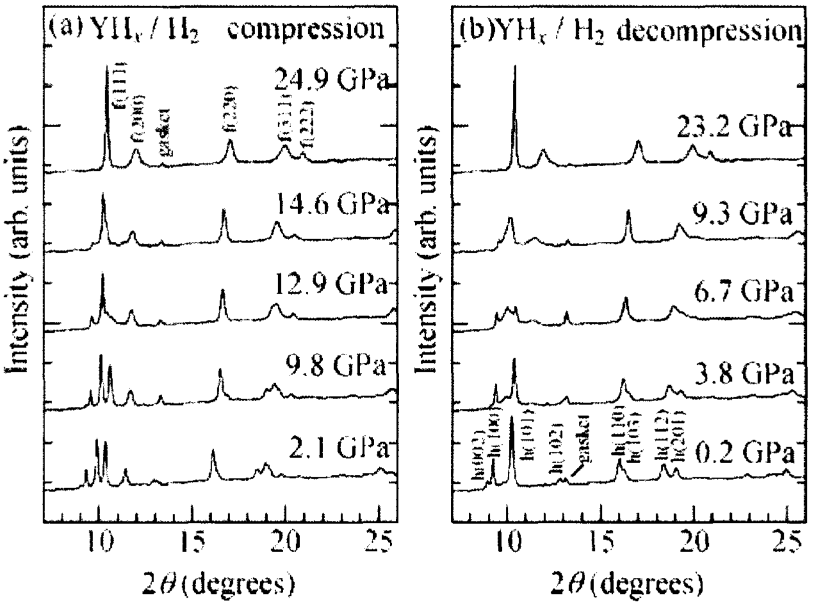

Fig. 3.6: X-ray diffraction patterns measured for YH_3 [5] which shows yttrium's structure changes hcp to fcc upon compression.

Fcc phase is stable up in high-pressure range. The intermediate state while in the above pressure range has been interpreted as the coexistence of the low-pressure hexagonal and high-pressure cubic phases. In Fig. 3.7, powder diffraction profiles are simulated for various candidate structural models by systematically changing the numbers of hexagonal-type (*ABA*-type) and fcc-type (*ABC*-type) layers contained in a unit cell. The intermediate state was a single phase and their diffraction patterns were well reproduced by models with long period stacking structures of Y metal layers which arranged in ABA-type (H-type) and ABC-type (K-type) stacking sequence. In pressure region at 14 GPa, structure of the sample has a 4-H and 5 K-layer sequence, which were stacked up along the 3-fold axis. The 17.9 GPa structure was described with consisted of a 2-H and 7-K layer sequence. The K-type component increased in number gradually with increasing pressure, and eventually become the only type lead to fcc phase. The interstitial H atoms likely played a dominant role in the formation of the long period structure.

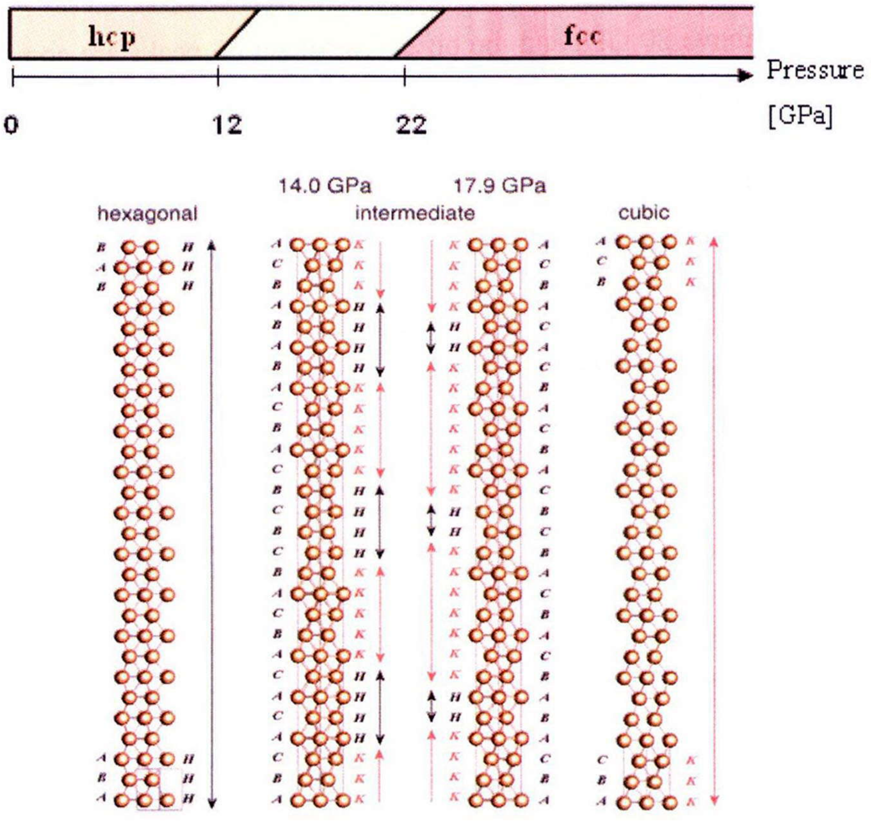

Fig. 3.7: Schematic illustrations of the long-period structures of the yttrium sublattices at 14.0 and 17.9 GPa. The hexagonal and cubic structures are also shown [5].

3.2.3 Optical property

Using a diamond anvil cell (DAC), the infrared spectra of YH_3 were measured under high pressure [3,6]. The visible color change is shown in Fig. 3.8. The sample is yellowish transparent at 6 GPa, but the transmission shifts towards the red at 20 GPa to finally disappear completely at 24.8 GPa. The transmission spectra are shown in Fig. 3.9. Optical transmission spectra show that the semiconductor gap remains open until at least 25 GPa. The resulting pressure dependence of the optical gap E_g is shown Fig. 3.10. Extrapolating the pressure dependence of the gap, an insulator to metal transition is expected at 55 ± 8 GPa.

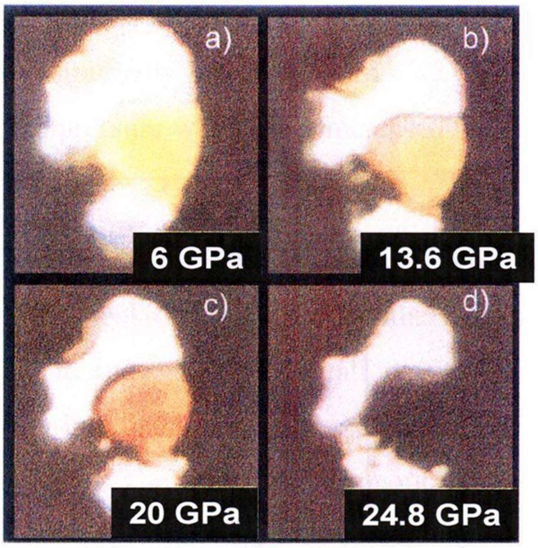

Fig. 3.8: Transmission photographs of YH_3 at high pressure in a DAC [3].

Transmission photographs of 500-nm thick YH_3 films at high pressure in a DAC. There is sample in the centre of the picture of the gasket hole which is filled with H. Images are taken at 6 GPa (a), 13.6 GPa (b), 20 GPa (c) and 24.8 GPa (d). The sample is yellowish transparent (a) at low pressure, but the transmission shifts towards the red (b and c) to finally disappear completely from the visible spectrum (d).

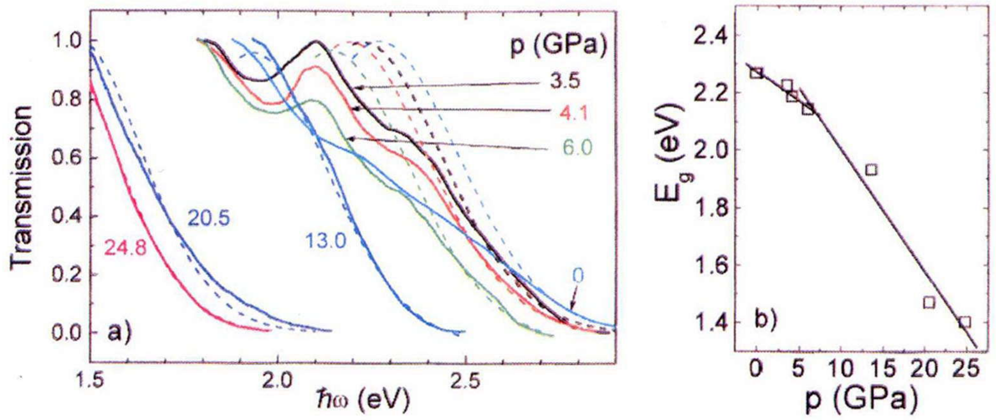

Fig. 3.9: Experimental transmission spectra of YH_3 under high pressure at various pressures [3].

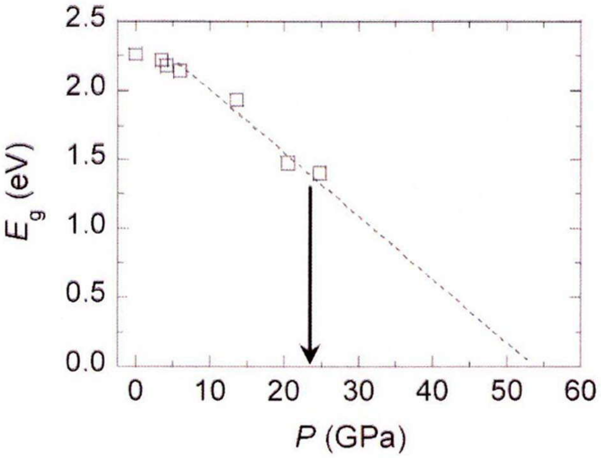

Fig. 3.10: Pressure dependence of the energy gap measured by the visible absorption measurement [3]. The resulting pressure dependence of the optical gap *E.* The latter fit extrapolates to a zero gap at 55.68 GPa, where an insulator-to-metal (IM) transition is expected to take place.

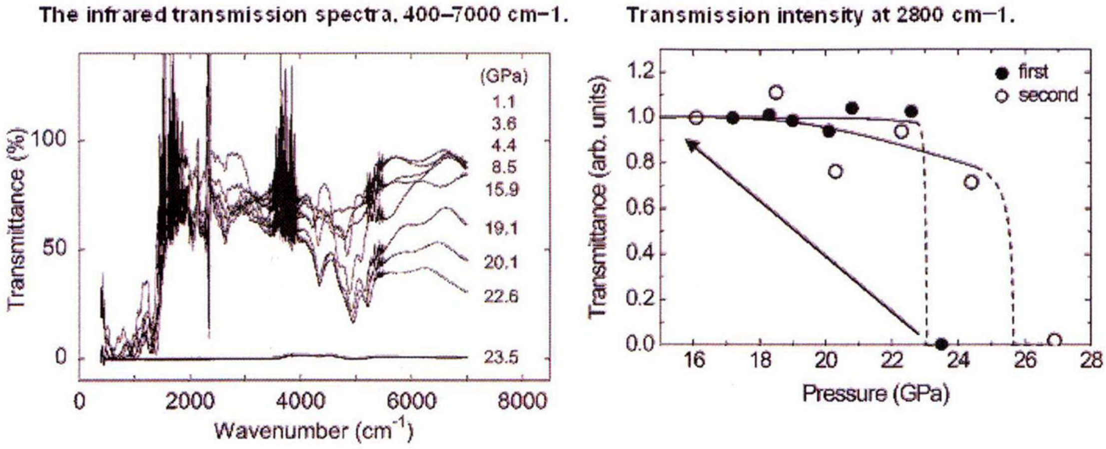

The infrared transmission spectra. 400–7000 cm−1.

Transmission intensity at 2800 cm−1.

Fig. 3.11: Metal transition is expected at around 24 GPa.

(a) Transmission spectra measured at various pressures. Transmitted light was completely lost in the whole infrared region at 23.5 GPa.

(b) The transmission intensity remained nearly constant as the pressure was gradually increased from 17.2 to 22.6 GPa and dropped to zero as the pressure was further increased to 23.5 GPa.

Fig. 3.11a shows the transmission spectra expanded over the entire infrared region. The absorption peaks in the wave-number regions of 400–1200 and 4000–5000 cm^{-1} were due to the hydrogen vibrations of YH_3 and H_2, respectively. The absorption due to the interband electronic excitations was not observed at pressures roughly below 16 GPa. The spectrum dramatically changed when the pressure increased from 22.6 to 23.5 GPa. The transmission spectrum abruptly collapsed over the entire infrared region. The optical gap closed. The abrupt closing of the band gap is more pronounced in Fig. 3.11b where the relative transmission intensity at a fixed wave number of 2800 cm^{-1} is plotted as a function of pressure. The transmission intensity remained nearly constant as the pressure was gradually increased from 17.2 to 22.6 GPa and dropped to zero as the pressure was further increased to 23.5 GPa. The transparent sample was recovered when the pressure was decreased to 16 GPa. A rapid drop in intensity was again observed in the second compression at a pressure between 24.4 and 26.9 GPa. The transition pressure slightly shifted to a higher pressure since the sample probably suffered from some degradation during the compression and decompression cycles.

Comparing this result with in ref [3], that showed that the energy gap remained up to 25 GPa, while the present infrared measurements indicated that the gap closure was at 23–26 GPa. This discrepancy is probably explained by the sample conditions. In the visible measurement, the hydride was prepared by evaporating a thin film of yttrium metal, which was 0.5 μm thick, on the top surface of a diamond anvil, and hydrogenating the film with hydrogen fluid under pressure. Thus, the thin film that evaporated on the diamond may suffer from nonhydrostatic stress during compression due to the significant mismatch in the compressibility between the hydride and diamond. However, in the present study the self-standing hydride foil was pressurized in hydrogen fluid/solid under hydrostatic or nearly hydrostatic conditions and probably underwent an insulator-metal transition at slightly lower pressures.

3.3 Experimental Results

3.3.1 Raman spectrum

After loading H_2, sample was used to measure Raman spectrometer at 3 GPa as shown in Fig. 3.12. The Raman measurements were performed at room temperature. The laser beam of 532 nm was focused on an area of the sample. We compare the spectrum of this study with those of A.M Carsteanu's. [27]. Raman lines are compatible with sample YH_3 for the *hcp* structure which indicating the stoichiometry of H is close to 3.

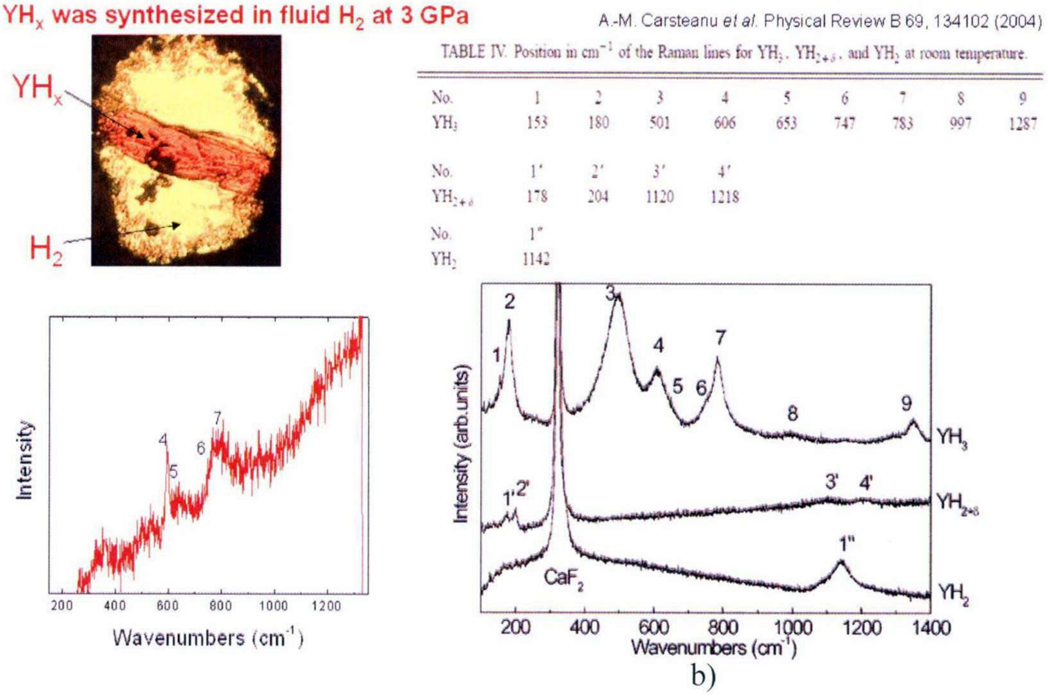

A.-M. Carsteanu *et al.* Physical Review B 69, 134102 (2004)

TABLE IV. Position in cm^{-1} of the Raman lines for YH_3, $YH_{2+\delta}$, and YH_2 at room temperature.

No.	1	2	3	4	5	6	7	8	9
YH_3	153	180	501	606	653	747	783	997	1287
No.	1'	2'	3'	4'					
$YH_{2+\delta}$	178	204	1120	1218					
No.	1"								
YH_2	1142								

Fig 3.12: a) Typical Raman spectrum of YH_3 at 3 GPa obtained in this work.
b) Typical Raman spectrum of YH_3 of A.M.Carsteanu in [27]

3.3.2 Pressure dependence of electrical resistance at room temperature

- YH_3 undergoes a structural transformation from the hexagonal hcp to cubic fcc via an intermediate phase under high pressure [26] under high pressure. To observe I-M transition by the direct measurements of resistance in DAC, pressure dependence of the resistance at room temperature were measured as shown in Fig. 3.13.

- We observed two maximums in the ρ-P curve at around 12 and 40 GPa, which is consistent to our previous results [13]. The first maximum may correspond to the appearance of the intermediate phase with long period stacking structures of yttrium. According to the x-ray structural studies, [26] no change in the structure by yttrium atom at the vicinity of the second maximum. This anomaly may be related to rearrangement of the hydrogen at the pressure range, however determination of the position of hydrogen atoms in the yttrium lattice is hardly possible at the high pressure. After the first maximum, the resistivity showed logarithmical decrease in the intermediate phase, which indicated the gradual appearance of a high conductive, metallic phase, but the resistivity kept decreasing up to the highest pressure of 75 GPa. Previous infrared transmission measurement showed a sudden transition to metallic phase at around 23 GPa [15], showing a disagreement with the present results. Another optical measurement claimed that metallization is expected with a continuous gap closing at 55 ± 8 GPa [3]. We confirmed that YH_3 sample show color change in transmission as shown in Fig. 3.14. The sample is yellowish transparent at 1.59 GPa, changes the red at 9.95 GPa and finally to appear black color at 11.38 GPa.

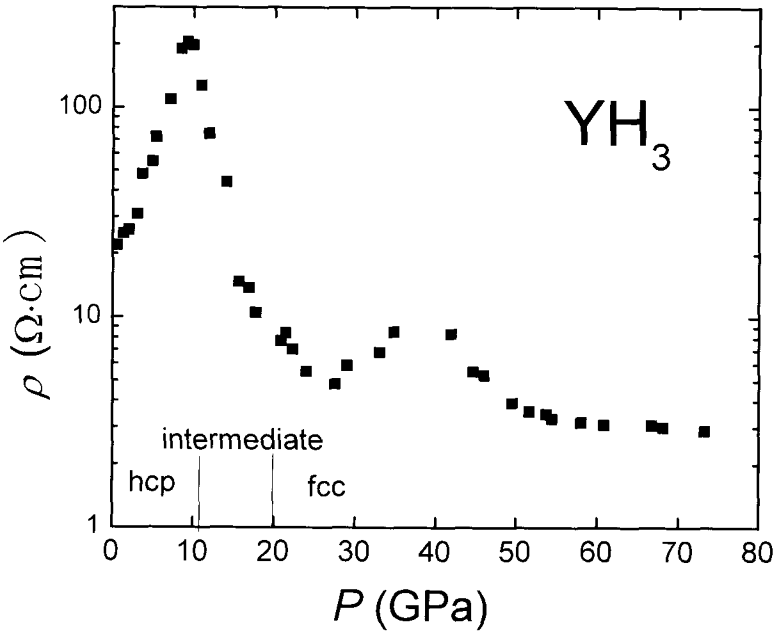

Fig. 3.13: Pressure dependence of electrical resistance at room temperature in YH_3. A structural transition from hcp to fcc around 12 GPa.

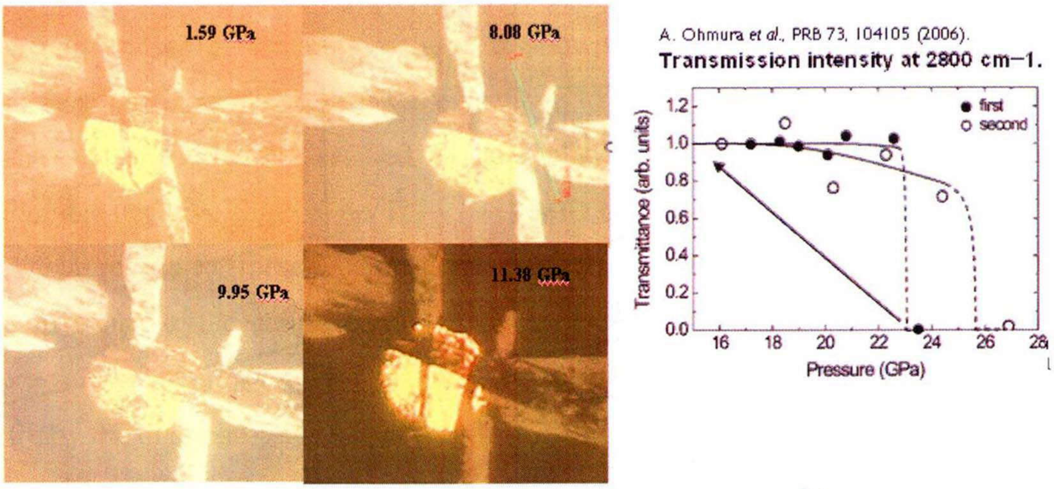

a) b)

Fig. 3.14: Transmission photographs of YH_3 at high pressure in a DAC
The sample was observed yellowish transparent at 1.59 GPa to become black color at 11.38 GPa.

3.3.3 Temperature dependence of electrical resistance

We measured the resistivity as a function of temperature at fixed pressures at low temperature and the typical results are shown in Fig. 3.15. The temperature dependence of the resistivity was negative slope ($d\rho/dT < 0$) at pressures below 50 GPa and became almost independent to temperature above 74 GPa, which indicates the onset of metallization took place at pressure range from 50 to 74 GPa.

We calculated ΔE_g with equation (1). The band gap seems to close to zero at pressure about 90 GPa and I-M transition occurs in YH_3.

$$\sigma(T) \approx \sigma_0 \exp[-\frac{\Delta E_\sigma}{k_B T}] \qquad (1)$$

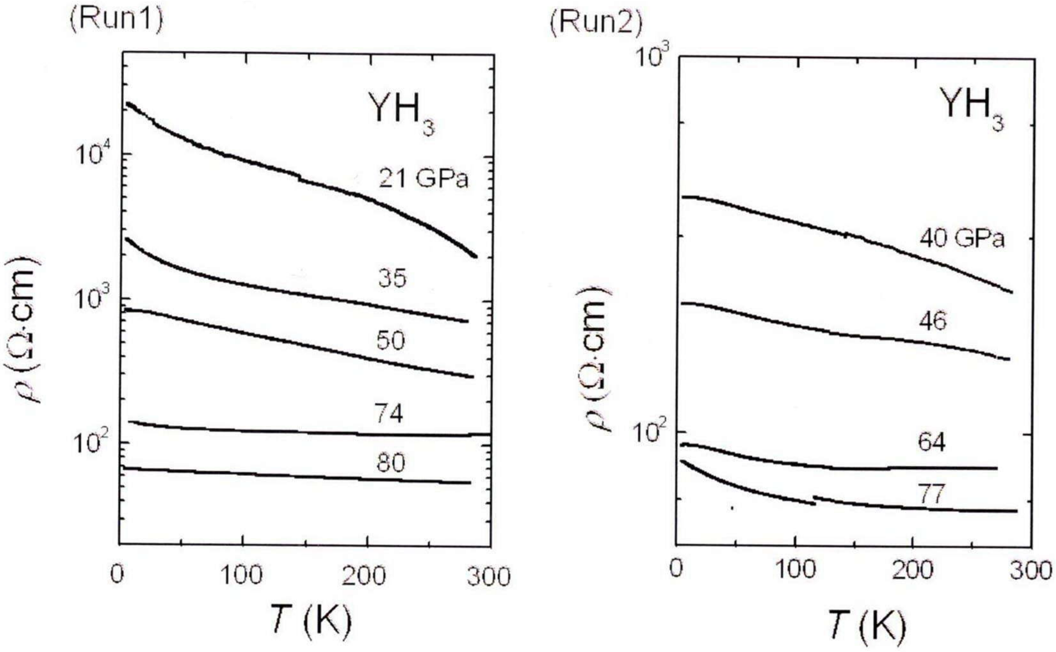

Fig. 3.15: The temperature dependence of the electrical resistivity at different pressures.

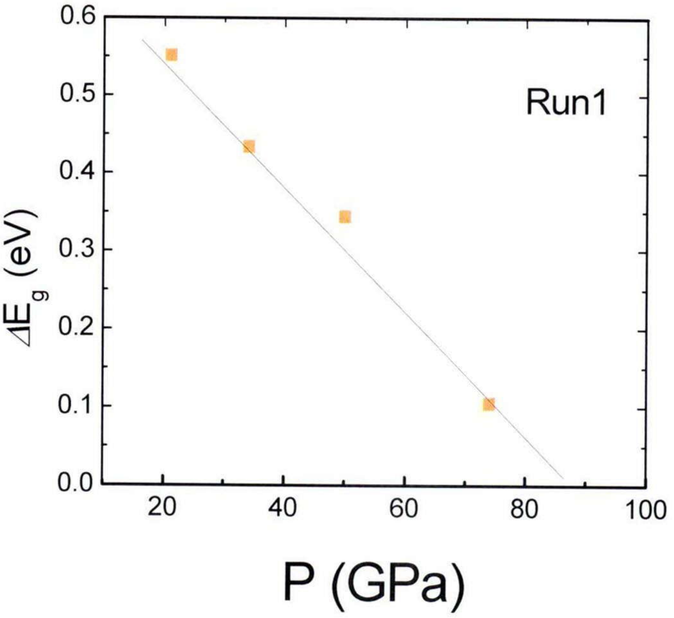

Fig 3.16 Band gap will to be closed to zero at pressure about 90 GPa.

We compare the results of this study and the previous measurement of resistance versus temperature in our lab as discussed in [13]. The plot of the resistance versus temperature at several pressures is shown in Fig 3.17. Semiconducting or insulating behavior of the sample was evident up to 4.4 GPa. With increasing pressure, the onset of metallization seemed to take place at pressure of 44 GPa by the considerable negative slope of $d\rho/dT$.

The reason for these discrepancies is not yet understood, however may be due to the difference of the sample condition under pressure, such as nonhydrostatic stress. No pressure medium was used in our experiment and the sample was pressurized directly by the diamond-anvil surface. In fact ρ-T curves in our number of experiments shows slightly different in each runs. In addition the previous samples in the optical measurements were surrounded by hydrogen at pressure. As the result of the stress and the lack of hydrogen, the number of hydrogen (value of x in YH_x) may be slightly smaller than 3 and the sample became inhomogeneous and semiconducting parts may remain even at high pressure.

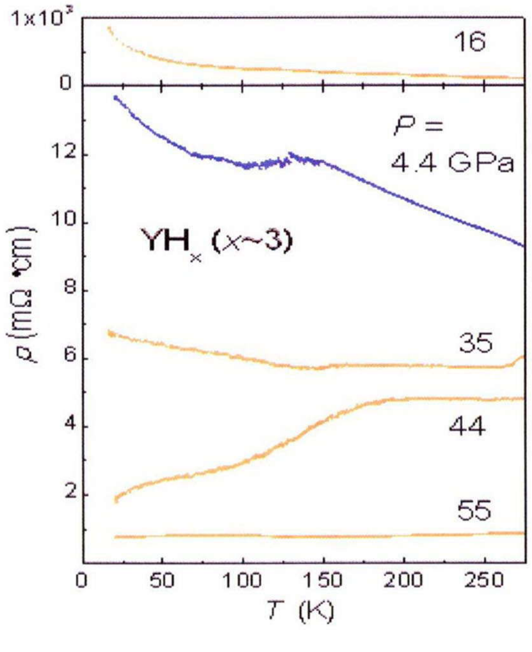

Fig. 3.17: The temperature dependence of electrical resistance at difference pressure.

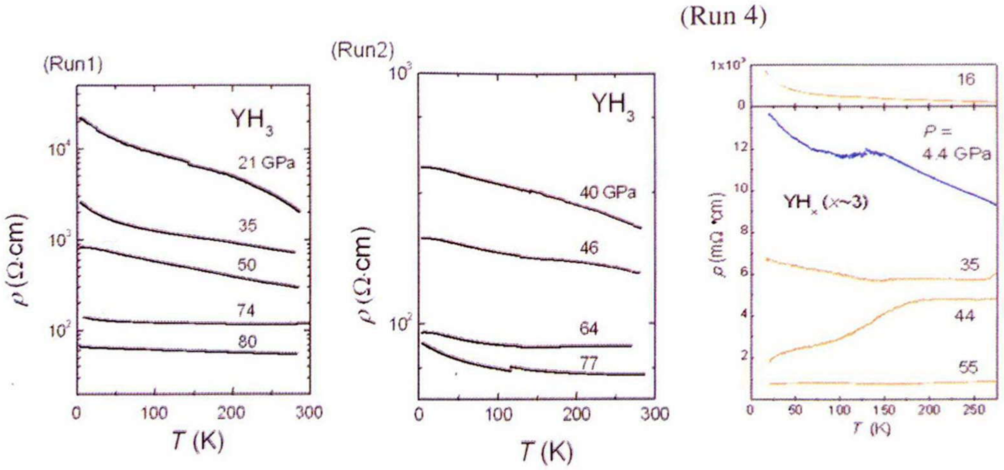

Fig. 3.18: Variety of R-T curves

- metallization expected around 70 GPa in Run 1 and above 80 in Run 2
- metallization occurs around 40 GPa in run 4

In Fig. 3.18, there show variety of R-T curve. That different is formed from hydrogen content and pressure condition different. Here I did my best for keeping with the same pressure condition. So that, those results are only depend on hydrogen content. Upon investigation of the M-I transition in these metal hydrides would not to be complete without a detailed study of the insulating $YH_{3-\delta}$ with very small δ. But YH_3 is sensitive with δ under high pressure.

Schematic drawing of the variety of stoichiometry of hydrogen in $YH_{3-\delta}$ is to show in Fig. 3.19. This may caused by deferent condition of the synthesis of hydrides such as thickness of metal, time, and pressure.

Even the semiconducting character remained at pressures above 50 GPa, the resistance showed a small drop with decreasing temperature around 10 K by increasing the measuring current from 10 μA to 1 mA. A shown in Fig. 3.20 we determined the critical temperature, T^* where the ρ-T curve deviated from the trends of semiconductor and plotted T^* as a function of pressure in Fig. 3.21. The value of T^* is rather closed the superconducting transition temperature of theoretical prediction [2], however no magnetic field dependence of T^* was observed.

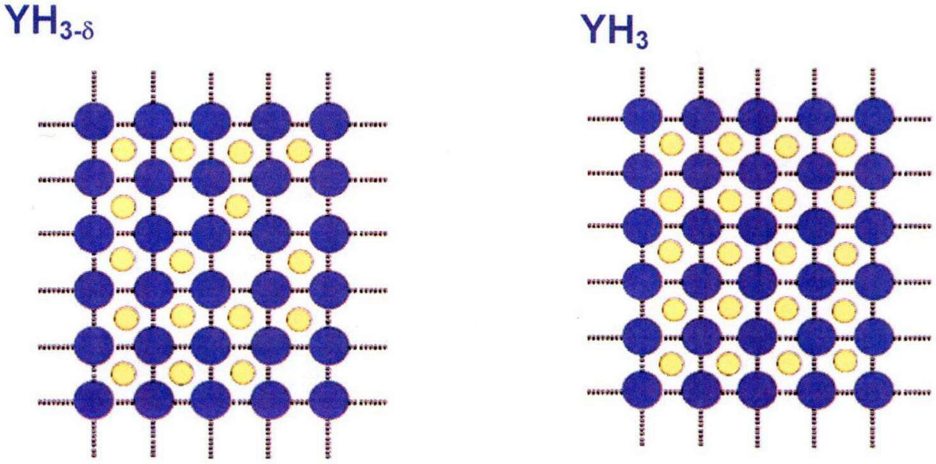

Fig. 3.19: Schematic drawing of the variety of stoichiometry of hydrogen in $YH_{3-\delta}$.

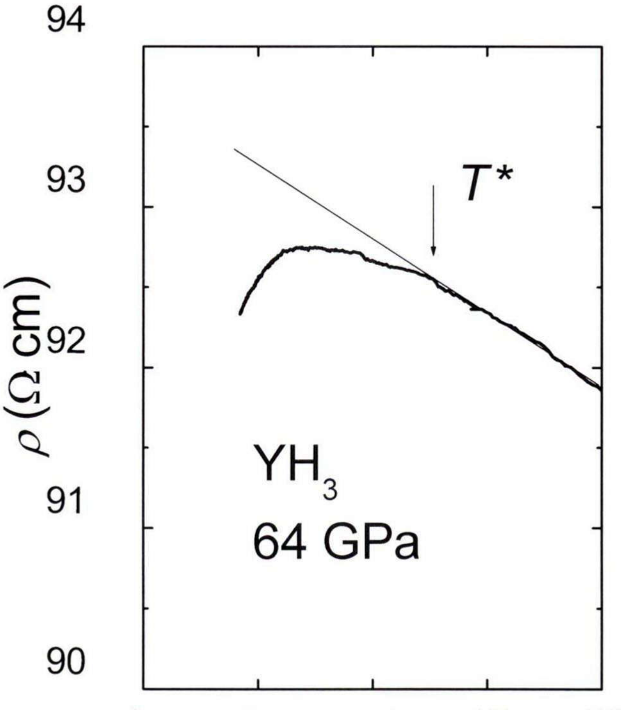

Fig. 3.20: The small resistance drop at low temperature. The line shows a trend of semiconducting curves observed at higher temperature. The arrow indicates the T^*.

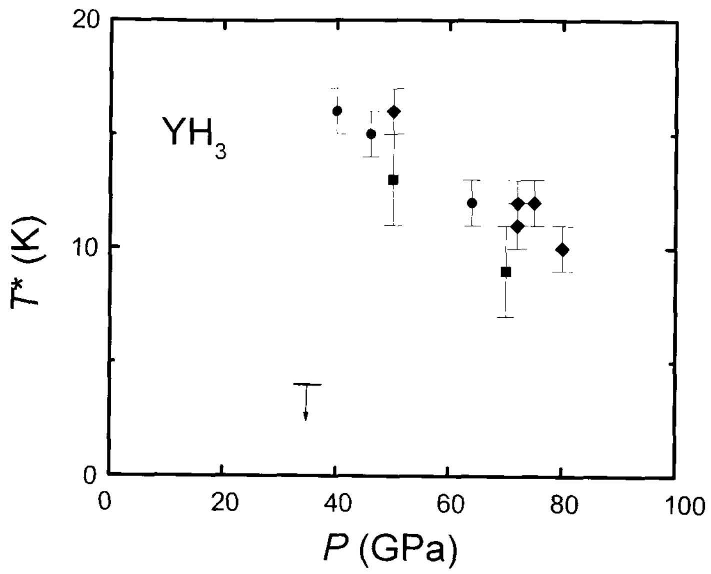

Fig. 3.21: Pressure dependence of the transition temperature T^* of YH_3.

We observed pressure-induced metallization in metal-hydride system, YH_3. The result should be important step towards understanding underlying physics of hydrogen rich system.

3.3.4 Photoconductivity

Photoconductivity is an optical and electrical phenomenon in which a material becomes more electrically conductive due to the absorption of electromagnetic radiation such as visible light, ultraviolet light, infrared light, or gamma radiation.

Transparent orange yttrium hydride turns to black when illuminated by visible laser light at pressures of several gigapascals at room temperature. The marked reduction in optical transmittance extends over the infrared region, suggesting that illumination creates persistent free carriers. The black sample returns to the transparent orange hydride during room-temperature annealing for a few hours as shown in Fig. 3.22. Photochromism is pronounced for the coexistent state of the metallic fcc-YH_2 and the insulating hexagonal-YH_3 state but is depressed for the single phase of hexagonal-YH_3 as discussed in [6]. These results indicate that light illumination can modify the optical and possibly electronic properties during a certain period of times the metal-insulator transition by hydrogenation.

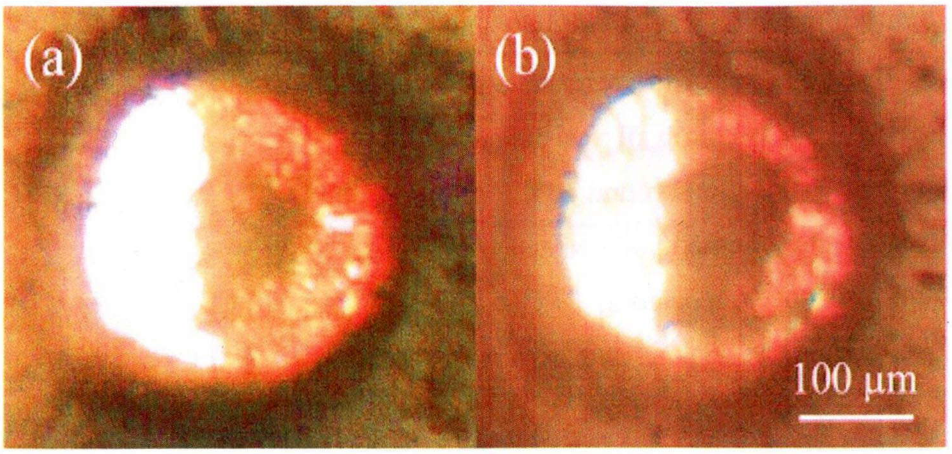

Fig. 3.22: The radiated part turns opaque black immediately by 5 seconds illumination with the 488 nm light from an Ar ion laser [6].

Our hydride sample was synthesized by hydrogen of pure yttrium in fluid H_2 at a pressure of 3 GPa. We manifested significantly enhanced conductivity in the semiconducting YH_x upon illuminated by visible light. We attribute the enhance conductivity resulting from illumination by visible light to the following mechanism:

- Creation of free charge carriers.
- Inter band transition of electrons, existence of a donor level below the conduction band edge; Deabsorbtion and recombination of H.
- Enhanced mobility of H and vacancy; Heating effect.

The result demonstrate a potential switch able function controlled by light illumination, which is close with resistance of sample increases gradually and eventually resumes the initial value within a large relaxation time. A illuminating with different light from another Argon gas laser, respectively λ = 514, 488,1064 nm in laser power 0.3mW, which was focus to on the sample surface, immediately change the resistance, as show Fig. 3.23. The resistance of sample drops rapidly and become saturated within 10 minutes. Once the laser is switched off, resistance increases gradually and eventually resumes the initial value within a large relaxation time. There are the same the laser power density and pressure at difference wavelength. The green light illumination can induce 40% drop of resistance at 1.6 GPa, the blue light is induced 60 % drop of resistance and 2% drop of resistance for red light. This is likely due to the interference effects the long wave light, which can pass through the transparent. The sample was illuminated buy the 514 nm argon laser for 10 min. The green light illumination can induced 40% drop of resistance at 1.6 GPa. During apply pressure, the reduction of the resistance decreased above 50%. The illumination gets small effect with 8% drop of resistance at 11.49 GPa. There is the occurrence a structural phase transition around 10 GPa. This result is confirmed through the in situ high-pressure measurement of resistance using the DAC at room temperature. The maximum resistance expected at 10 GPa and start change phase transition from hcp-fcc as shown in Fig. 3.25.

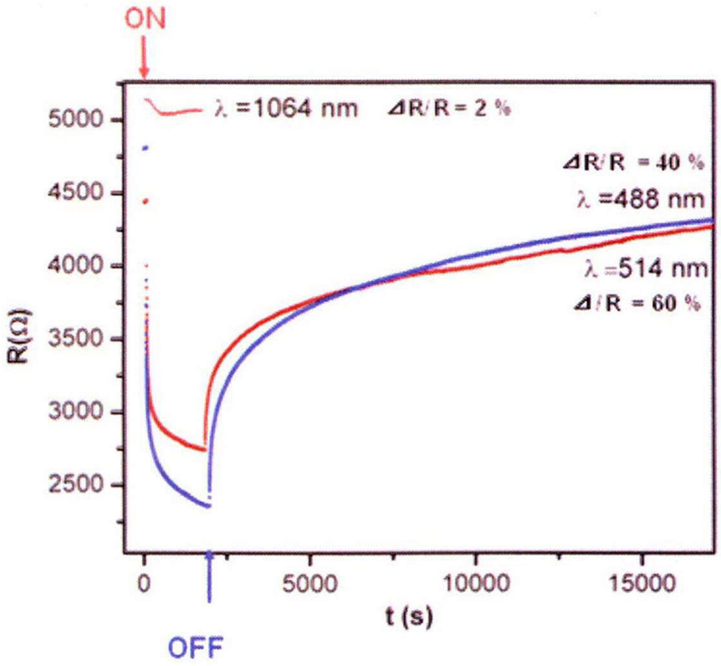

Fig.

ble light.

green light
λ = 514 nm

blue light
λ = 488 nm

red light
λ = 1064 nm

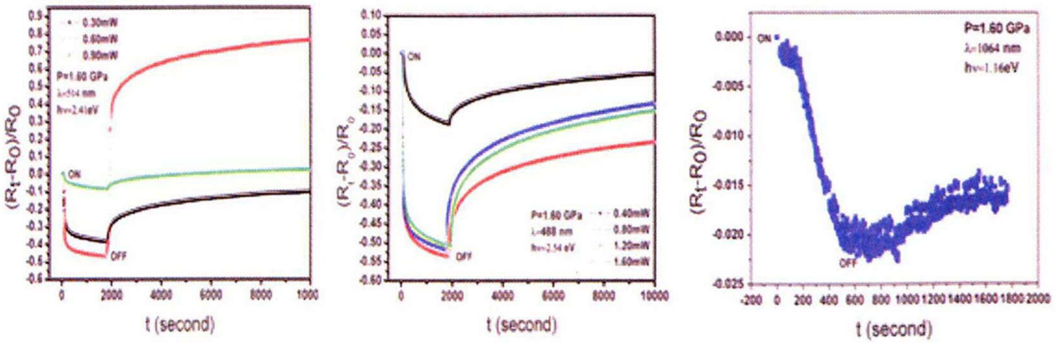

Fig. 3. 24: Time-dependence of the resistance of YH_3 illuminated by visible light with different laser power density.

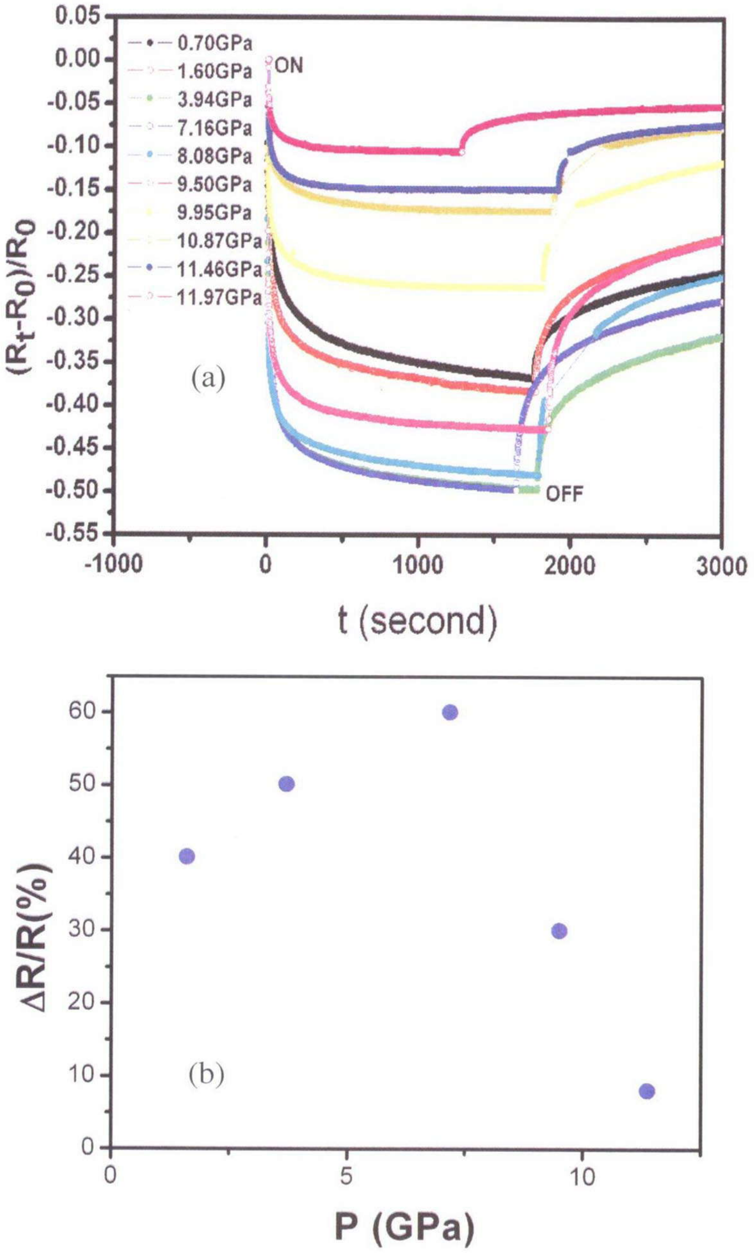

Fig. 3.25: Time-dependent resistance of YH_3 illuminated by visible light with difference pressures (a). Pressure dependence of resistance drop by visible light (b).

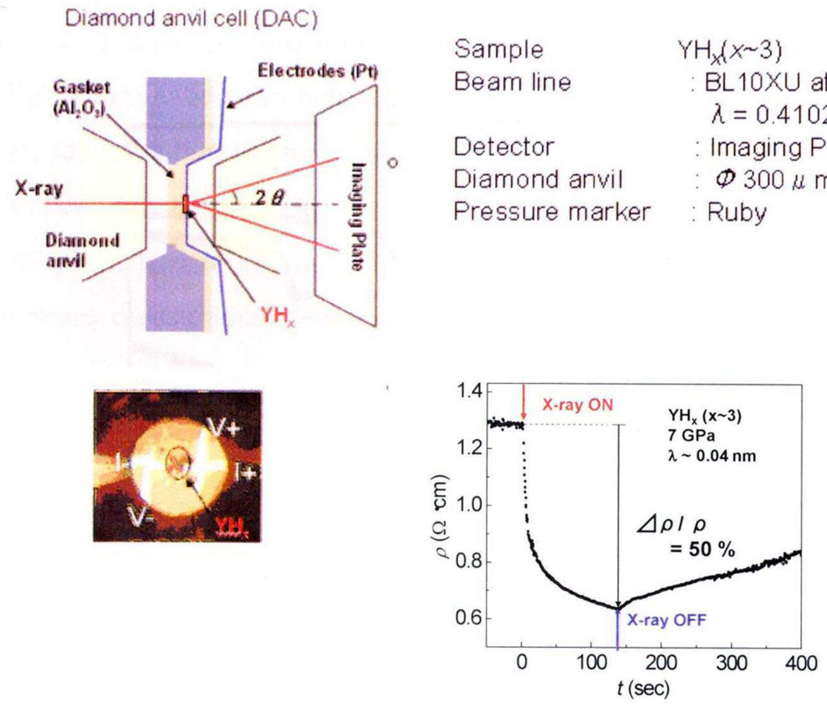

Sample	YH_x(x~3)
Beam line	: BL10XU at SPring-8 λ = 0.4102 Å
Detector	: Imaging Plate
Diamond anvil	: Φ 300 μ m
Pressure marker	: Ruby

Fig. 3.26: Photo-induced conductivity of YH_3. measured resistance and structure at the same time at Spring-8 (a). Time- dependent resistance of YH_3 illuminated by X-ray at room temperature (b). X-ray ON, resistance drops rapidly; X-ray OFF, resistance increases gradually and eventually resumes the initial value within a large relaxation time.

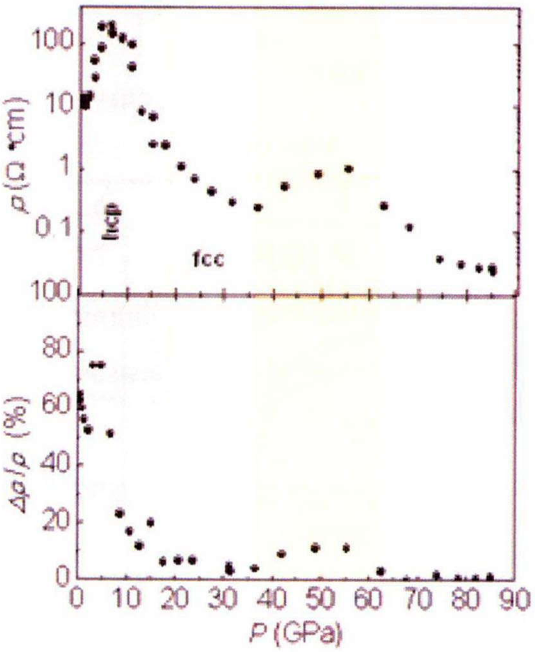

Fig. 3.27: Pressure dependence of resistance under illumination by X-ray in DAC.

X-ray also affects the conductivity in YH_3 obviously. The resistance decreased about 50% by X-ray illumination as shown in Fig. 3.26. The pressure dependence of the resistance is shown in Fig. 3.27.

One possible mechanism is the site-to-site hydrogen transfer, the photon energy dependence of photochromism. The light illumination can modify the optical and electronic properties.

3.4 Summary

Hydrogenation causes yttrium to exhibit a metal-insulator transition. Structural transformation from the original hexagonal to the fcc cubic structure under high pressure. We observed pressure-induced metallization in metal-hydride system, YH_3. But we note that variety of hydrogen content may cause variety of conductivity. No superconductivity was observed up to 80 GPa. The result should be important step towards understanding underlying physics of hydrogen rich system.

References

[1] J. N. Huiberts *et al.*, Nature, 380 (1996) 231

[2] R. Ahuja et al, Appl, Phys, Lett, 71, 3498 (1997)

[3] R. J. Wijngaarden et al, Journal of alloys and compounds 308 (2000) 44-48

[4] T. Palasyuk and M. Tkacz, Solid State Commun. 130, (2004) 219.

[5] A. Machida, Solid state communiations 138 (2006) 436-440

[6]. A.Ohmura *et al.,* Appl. Phys. Lett. 91 (2007) 151904

[7] D. Y. Kim *et al.*, Phys. Rev. Lett., 103 (2009) 077002

[8] A. Van Geest-Lokhorst, Thesis 2006.

[9] A. Remhof, Thesis 1999, Hydrogen in Ytrium films

[10] P. Vajda, J. N. Daou, A. Lucasson, and J. B. Burger, J. Phys. F 17 1029 (1987).

[11] Y.K Vohra, Phys, Rev, Lett, Vol.47, No.15, 12 Oct 1987

[12] P.J. Kelly et al, Phys, Rev, Lett, 78, 1315 (1997)

[13] T. Matsuoka. J.Phys.Jpn.76 (2007) Suppl. A, pp. 86-87.

[14] J. S. de Almeida *APL* 94, 251913 (2009)

[15] A. Ohmura, *et al...,* Phys. Rev. B, 73 (10): 104105, 2006

[16] R. Griessen, Europhysics News (2001) Vol. 32 No. 2

[17] J. J. Hamlin, *et al...,* Phys. Rev. B, 73 (9): 094522, 2006.

[18] S. Lei, *et al...,* Phys. Rev. B, 75 (2): 024512, 2007

[19] Z. P. Yin, *et al...,* Phys. Rev. B, 74 (9): 094519, 2006

[20] T. Kume, *et al...,* Phys. Rev. B, 76 (2): 024107, 2007.

[21] C. Probst and J.Wittig. *Handbook on the Physics and Chemistry of Rare Earths edited by K. A. Gschneidner, Jr. and L. Eyring*. 1978. p. 749

[22] J. Wittig. *Phys.Rev. Lett.*, 24 (15): 812–815, Apr 1970

[23] D.Y. Kim, Digital Comprehensive Summaries of Uppsala Dissertations from the Faculty of Science and Technology 597

[24] N. W. Ashcroft. *Phys. Rev. Lett.*, 92 (18): 187002, May 2004.

[25] B. Philip, *Phys. Rev. B*, 6 (7):2577–2579, Oct 1972.

[26] A. Machida et al., Phys. Rev. B 76 (2007) 052101

[27] A.-M. Carsteanu *et al.* Physical Review B 69, 134102 (2004)

Chapter 4. High-pressure effect on perovskite hydrides

In this chapter, the studies of metallization and superconductivity in hydrogen-rich system of the cubic perovskite structure are described. We focus our attention to CaT-H_3 for T = Ni and Co at high pressure. These materials are not yet intensive studied under high pressure.

4.1 Basic Properties

4.1.1 Crystal structure

The perovskite-type hydrides is synthesized by solid-state reactions from the elements and binary hydrides at 673 -900 K at 1 – 20 MPa of hydrogen [13]. In this study, the perovskite-type hydrides were prepared by mechanical milling with 20 steel balls for 20-80 hours at 1 MPa of hydrogen at ambient temperature in hardened steel. In the sample preparation, there has the mount of elemental Fe contamination during the milling process, less than 0.3 mol %. The sample always handled in a glove box filled with purified helium or argon to avoid oxidation.

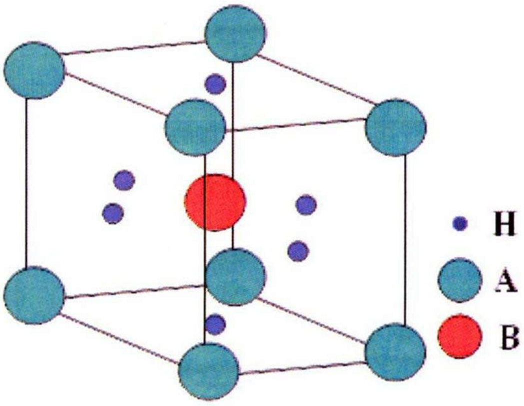

Fig. 4.1: The crystal structure of perovskite type hydride, ABH_3. A and B are cations and H is an anion.

Compound with perovskite structure are typically expressed as ABH_3, where A, B are cations and H is an anion. The idealized structure exhibits a primitive cubic unit cell with ions A at the corners, B at the centers, and H at the faced-centered positions of a unit cell composed of $[BX_6]$-octahedral and $[AX_{12}]$-cubo-octahedral. There are many perovskite-type hydrides reported in references [1-16].

The unit cell of $CaTH_3$ (T = Ni, Co, Fe, ...) identified as a cubic perovskite structure in space group Pm-3m. This hydride correlates with the characteristics of the transition metal's d-band. Ca atom places at the corner (0; 0; 0) and a transition metal atom in the center (0.5; 0.5; 0.5), where the tree additional hydrogen atoms are placed in octahedral sites at the face centers (0.5; 0.5; 0), (0.5; 0; 0.5) and (0; 0.5; 0.5) respectively. The precise atomic structure of $CaNiH_3$, schematically as shown in Fig 4.1, which was confirmed by the synchrotron X-ray diffraction measurement. The result of the X-ray diffraction measurements of $CaNiH_3$ is shown in Fig. 4.2. The X-ray diffraction pattern of hydrides Ca-Ni alloys could be index with a cubic unit cell a = 0.3553 Å [13].

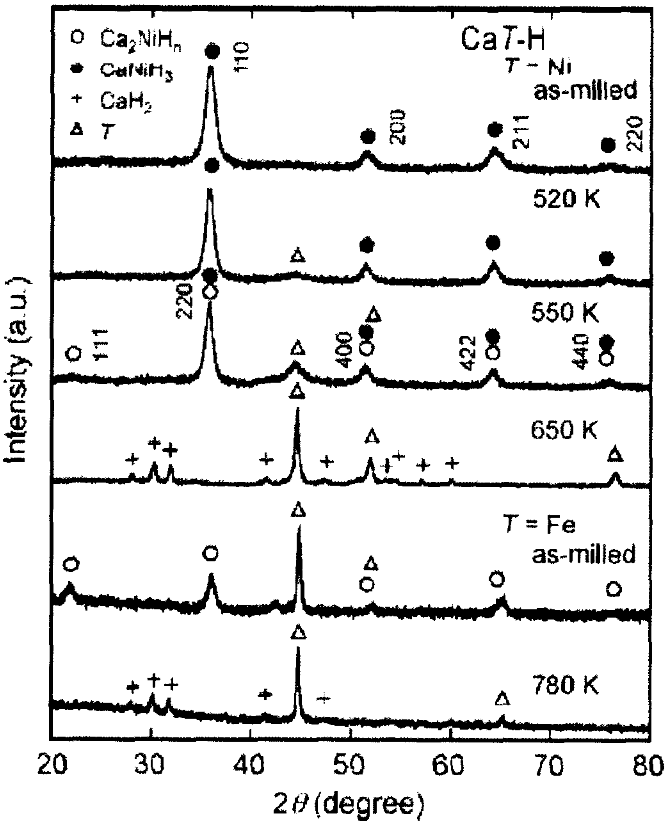

Fig. 4.2: X-ray diffraction profiles at ambient temperature of the as milled and heat treated CaT-H, T = Ni.

Table 2. Summary of crystal structure parameters of $Ca_{1+x}Ni–H$ for x = 0, 0.5 and 1.0 (space group Pm_3 no. 221) and Z = 1)

			x		
			0	0.5	1.0
Ca	1*a*	*g*	1^a	1^a	1^a
		B	1.2^a	1.2^a	1.2^a
Ni	1*b*	*g*	0.97(5)	0.85(4)	0.80(4)
		B	1.4^a	0.7^a	0.5^a
H	3*c*	*g*	1.09(1)	0.96(2)	0.95(2)
		B	2.1^a	2.5^a	2.8^a
a (nm)			0.35530(9)	0.35563(8)	0.35553(8)

4.1.2 The stability of the perovskite-type hydrides at ambient pressure

Compound with perovskite structure are typically expressed as ABH_3, where A, B are cations and H is an anion. In these coordinates, various perovskite-type hydrides plotted in Fig. 4.3. Here introduced is the Goldschmidt's tolerance factor, t, which is a geometrical factor to be commonly used for discussing the formation of perovskite-type oxides. The tolerance factor, t, is defined as,

$$t = \frac{R_A + R_H}{\sqrt{2}(R_B + R_H)} \qquad (1)$$

Where, R_A, R_H and R_B are the ionic radii of A, H and B ions, respectively. This factor provides necessary conditions for the formation ability of perovskite-type structure. In the present case, for convenience, (R_A+R_H) and (R_B+R_H) are replaced by the M-H interionic distance in the AH binary hydride and the B-H interionic distance in the BH binary hydride, respectively.

Every perovskite-type hydrides exists stably in the range of the t value from 0.9 to 1.16. If t is close to 1, the structure presumed to be closer to the ideal cubic unit cell. When the value of R_A is smaller than ideal and t is less than or equal to 0.81, many hydrides have slightly distorted variants with lower symmetry such as tetragonal, orthorhombic and triagonal lattices [17, 18].

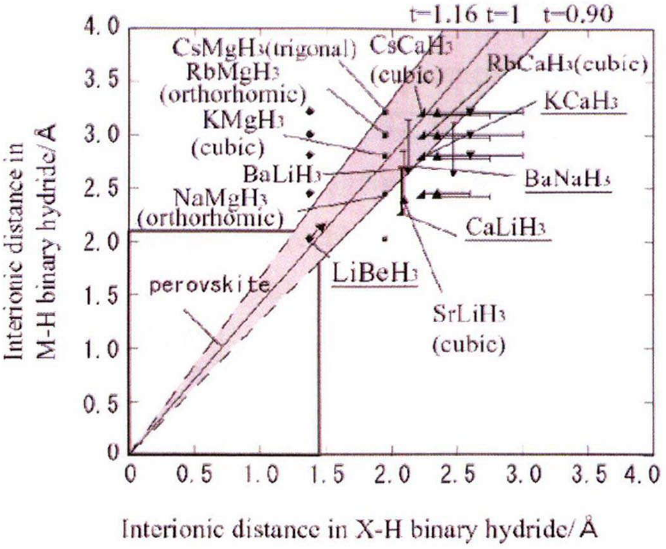

Fig. 4.3: Prediction for the stability range of perovskite-type hydrides, ABH_3, by the interionic distances in the binary metal hydride

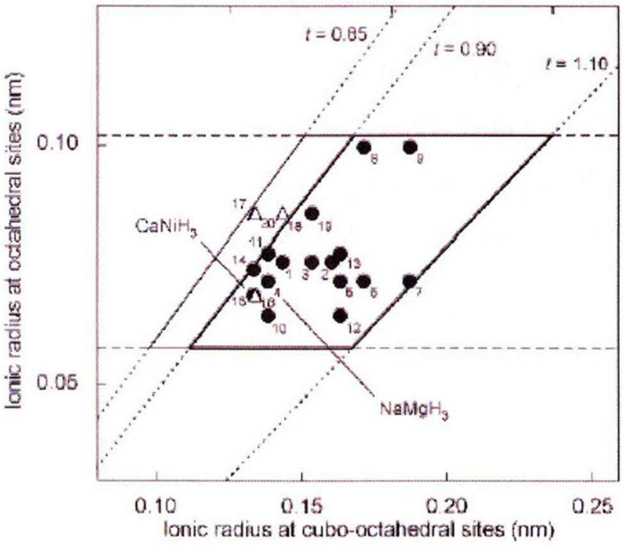

Fig. 4.4: Estimation of the formation abilities of provoke type hydrides using the Goldschmidt tolerance factor.

The detailed for estimation of the formation ability of the perovskite-type structures in Fig. 4.1. The perovskite-type structure is composed of [BH_6] octahedral and [AH_{12}] cubo-octahedral for the composition of ABH_3. On [BH_6] octahedral, the range of t for the perovskite-type hydrides with stoichiometric compositions (ABH_3) is narrow ($0.9 < t < 1.1$) than that for the perovskite-type oxides ($0.78 < t < 1.05$). This is instability in the anion state of hydrogen compared to that of oxygen due to the smaller value of its electronegativity. If hydrogen is stoichiometrically less than the perovskite composition ABH_3, the t values may tend to be smaller than 0.9. That the formation ability of perovskite-type hydrides can reasonably explain on the basic of the geometric restrictions on ions using the Goldschmidt tolerance factor. Fig. 4.4 compiles t for CaT-H_3 for T = Co, Ni and the t values for the systems realizing the Pm-3m structure fall in the range between 0.92 and 1.01, which is in agreement with the general observation. This justifies the ionic bonding description of this class of perovskite hydrides

4.1.3 Electronic structure

The band structure and DOS of $CaNiH_3$ are as shown in Fig. 4.5 and 4.6, respectively. The small lattice parameter of 3.5262 Å implies a wide dispersion of the hydrogen-based bands.

In $CaNiH_3$, the a_{1g}–e_g splitting of these bands pronounced. The lower lying a_{1g} band dispersed over a region from -10 to -6 eV below the Fermi level. This band contains a stabilizing contribution from the Ni-*s* state. Compared to the a_{1g} band, the e_g band is rather narrow and confined between -6.5 and -5.5 eV. Due to a substantial admixture of Ni e_g *d* states, this band is essentially responsible for Ni–H bonding. At -2 eV the dispersion, non-bonding, Ni t_{2g} *d* states centered. At even higher energies, from -1.5 to 1.5 eV, the Ni–H antibonding e_g band is distributed. This band is only half filled, which makes $CaNiH_3$ a metallic conductor. A completely filled e_g band would put the Fermi level at the pseudo-gap at 1.5 eV. The contribution of Ca states to the bands below the Fermi level is small. This suggests considering $CaNiH_3$ as consisting of a polyanionic framework $[NiH_3]^{2-}$ counterbalanced by Ca^{2+} cations.

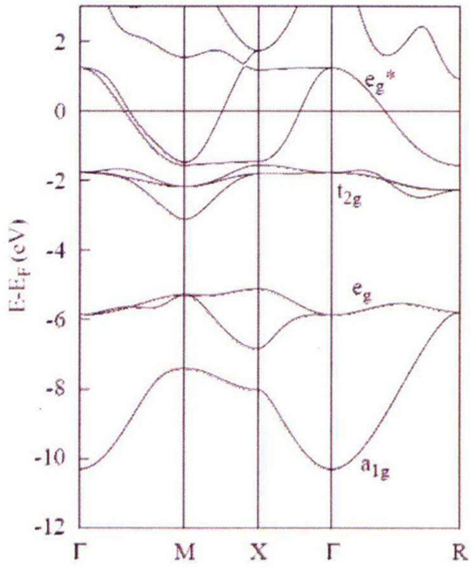

Fig. 4.5: Band structure of $CaNiH_3$ at the theoretical equilibrium volume.

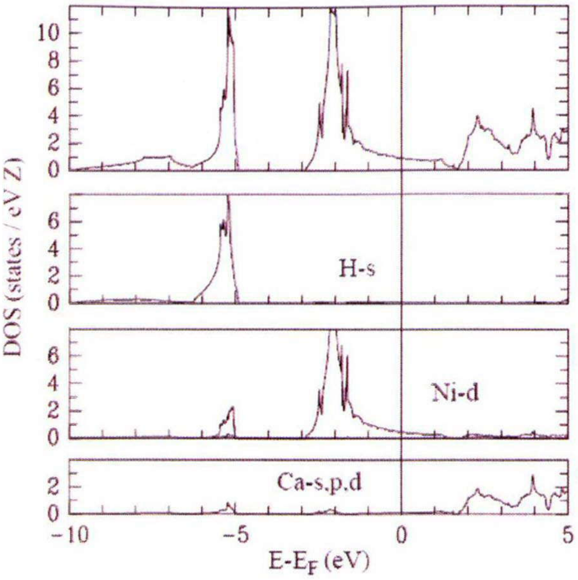

Fig. 4.6: Total density of states of $CaNiH_3$ and its decomposition into H-s, Ni-d and Ca-s, p, d contributions (from above).

4.2 Experimental and results

For many years, investigations on ABH_3 have been concentrated as hydrogen storage material. However, to investigate the electrical transport properties of samples under high pressure, we performed the electrical resistivity measurements at low temperature and high pressures up to 80 GPa using a four-probe method in a diamond anvil cell (DAC). The samples together with ruby chip as pressure marker were compacted in the sample chamber of gasket in the glove box to avoid the reaction with oxygen and moisture. We performed X-ray diffraction measurement on $CaCoH_3$ and $CaNiH_3$ at the pressures up to 83 GPa and 62 GPa, respectively at room temperature using synchrotron beam line BL10XU in the SPring-8.

4.2.1 Sample setting

Figure 4.7 shows our typical experimental setup in this study. $CaTH_3$ is highly reactive with water, oxygen and nitrogen. To avoid the chemical reaction and contamination of the sample, it kept inside a glove box filled with Ar-gas in Fig. 4.7.b. All procedures of the sample preparation and pressure cell loading carried out inside of the glove box. After loading sample, the pressure increased to some pressure to seal the sample chamber completely. To avoid any reactions between sample and surrounding materials, the pressure kept below 8 GPa at room temperature.

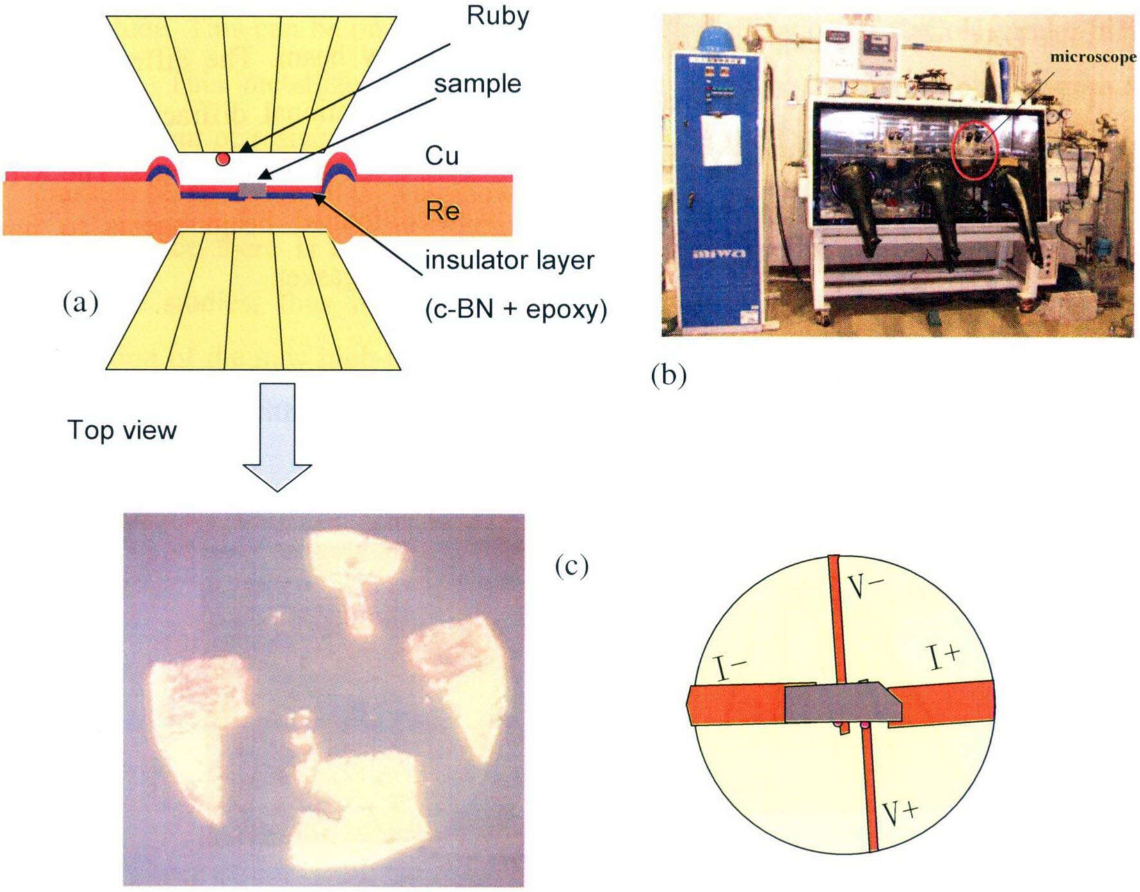

Fig. 4.7: Electrical resistance measurement in $CaTH_3$. (a) DAC setting: The culet of the diamond anvil: 300 μm; gasket material: Rhenium; thickness of gasket: 50 μm; insulator layer: c-BN powder +epoxy; electrode material: Cu (+Kapton thin film); pressure media: No; pressure marker: ruby.

(b) A glove box filled with Ar-gas.

(c) The top view of the setting for resistance measurement in DAC.

To investigate the electrical transport properties of samples under high pressure, we performed the electrical resistivity measurements at low temperature and high pressures up to 80 GPa using four-probe method in a diamond anvil cell (DAC) in Fig. 4.7a. The sample embedded on the thin film Cu electrodes on Kapton film without any pressure medium. The gasket made of c-BN and epoxy was covered by the Kapton film to avoid the chemical reaction. Ruby chip as pressure marker were compacted in the sample chamber.

The X-ray diffraction experiments carried out at beam line BL10XU of synchrotron radiation source SPring-8. Pressure medium was not be used as shown Fig. 4.8. X-ray passes through the optical window and the sample CaT-H_3 compressed in a DAC with the cell axis oriented along the X-ray beam. The diffracted X-ray patterns collected on a flat imaging plate (IP). Conventional diffraction diagrams obtained using PIP software via integration of the two-dimensional images. The X-ray wavelength was varied 0.413522 Å. The well-collimated beam seems to have contributed to avoid the obstacle intense diffraction from gasket.

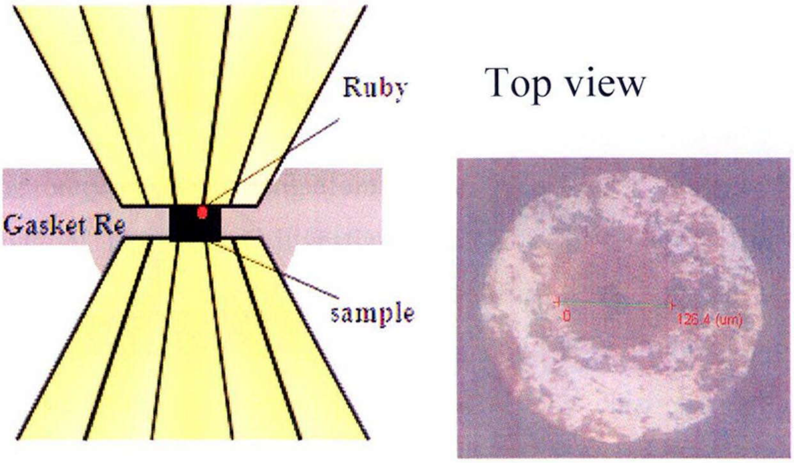

Fig. 4.8: The samples together with ruby chip as pressure marker were compacted in the sample chamber of metal gasket. The culet of the diamond anvil: 300 μm; gasket material: Rhenium; thickness of gasket: 50 μm; pressure media: No; pressure marker: ruby

4.2.2 Metallization of $CaCoH_3$

$CaCoH_3$ with perovskite-type structure has to show a non-metal with band gap about 1 eV. The ground state of $CaCoH_3$ is a nonmagnetic insulator with predominant electron configuration of d^6 of Co^{3+} fully occupying the t_{2g} level, exceeds the Hund's rule coupling energy in [3]. As shown in Fig. 4.9, the resistance of $CaCoH_3$ sample decreased up to 40 GPa and saturated above 40 GPa at room temperature. It is note that the resistance of the sample is semiconductor-like at ambient pressure, which decreases sharply in the pressure range of 10 - 40 GPa by about five orders of magnitude. This can be one of indication of the metallization of $CaCoH_3$ under high pressure. This metallized transition confirmed through the in situ high-pressure measurement of resistance versus temperature using the DAC, with the metallization pressure being above 40 GPa as shown in Fig. 4.10.

Since there is a phase transition at 40 GPa as discussed in the following structure studies, thus inferred that the resistance decrease were caused by the formation of the new high-pressure phase. When the pressure released, the resistance increases again with the same line when loading totally returns to ambient pressure.

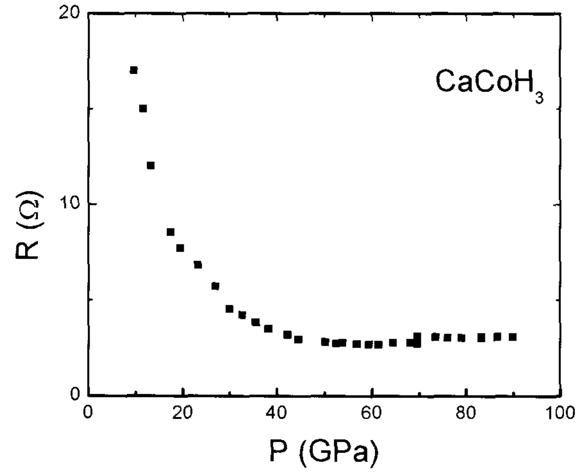

Fig. 4.9: Pressure dependence of electrical resistance at room temperature in $CaCoH_3$.

The electronic property seems to be reversible after pressure release. Here the crystal structure of transition phase is reversible or not change crystal structure during applying pressure.

The temperature dependence of electrical resistance was as shown in Fig. 4.10. The resistance increased with decreasing temperature at 17 GPa. This negative slope demonstrated semiconductor character. With pressure increasing, the absolute value of resistance decreased and the semiconductive behavior was effectively to suppress at high pressure. It is note that the *R*-*T* curve becomes almost flat at 40 GPa. Upon applying pressure, the *R*-*T* slope changed to positive up to 80 GPa, indicating the occurrence of metallization as the aforementioned measurements of resistance at room temperature. The results showed no superconductivity and small increase of the resistance at very low temperatures was observed.

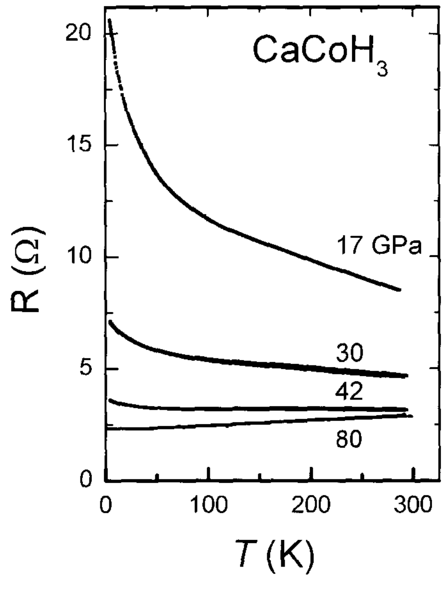

Fig. 4.10: Temperature dependence of electrical resistance at variety pressure.

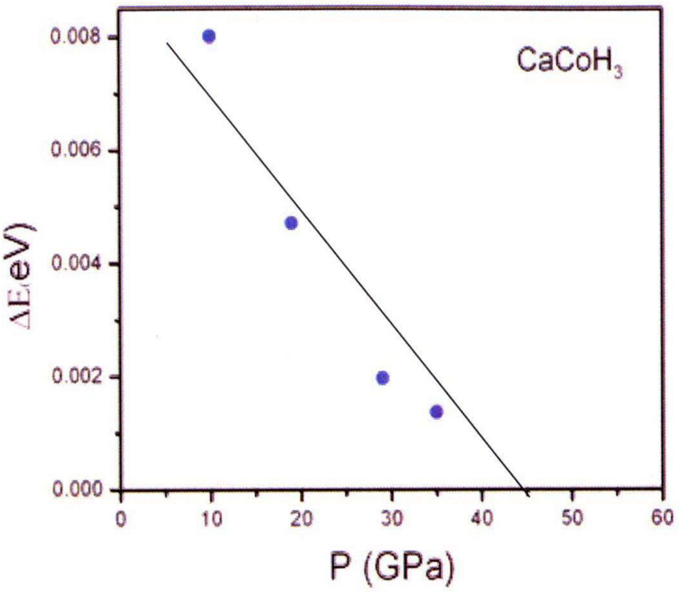

Fig. 4.11: The energy gap in CaCoH$_3$ will close at around 45 GPa.

As shown in Fig. 4.11, the gap which estimated by activation energy will close at around 45 GPa. The origin of this change in the resistivity at around 40 GPa will discuss in X-ray diffraction. Fig. 4.12 shows the spectra of X-ray diffraction results of CaCoH$_3$ at various pressures. The diffraction data collected in the pressure range 0.96 – 83 GPa. All of the obtained diffraction peaks were able to be indexed with previously reported fcc structures from Orimo group [13] with a lattice parameter of a = 3.5262 Å. The fcc phase maintained up to 83 GPa. There are seven peaks of the sample, indicated with (111), (110), (111), (200), (211), (220), (310) in the X-ray diffraction patterns. With pressure increasing, all peaks weakened gradually, and shifted to higher degree. The (111) peaks become weak and disappeared at 33.5 GPa, indicating that there maybe a crystal structure phase transition at 33.5 GPa. The (111) peak return to the original sites when the pressure was released from the maximum to ambient, so there is not the phase transition but deformation the crystal. The relationships of d values of peaks in pattern versus pressure are showing in Fig. 4.13. The d-value of fcc CaCoH$_3$ at ambient pressure are also included, indicating that CaCoH$_3$ does not decompose into CaCo and H$_2$ in the experiment pressure range. According to the peak intensity evolution and the d-value decreasing up to 83 GPa, the d value of the (111) peak is vanish at 33.4 GPa which indicates the deformation crystal of $CaCoH_3$ under high pressure.

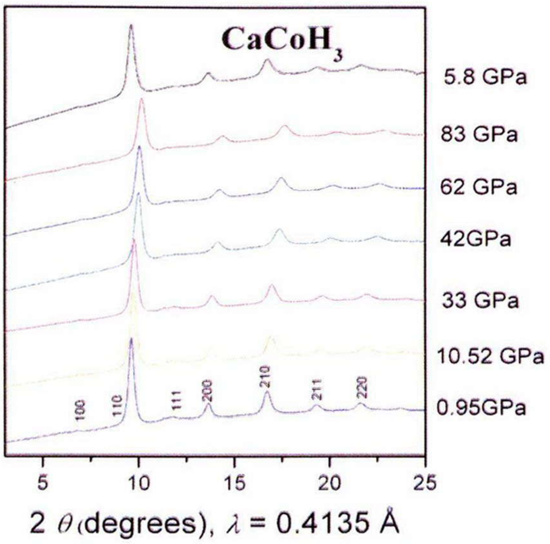

Fig. 4.12: X-ray diffraction patterns of $CaCoH_3$ at several pressures.

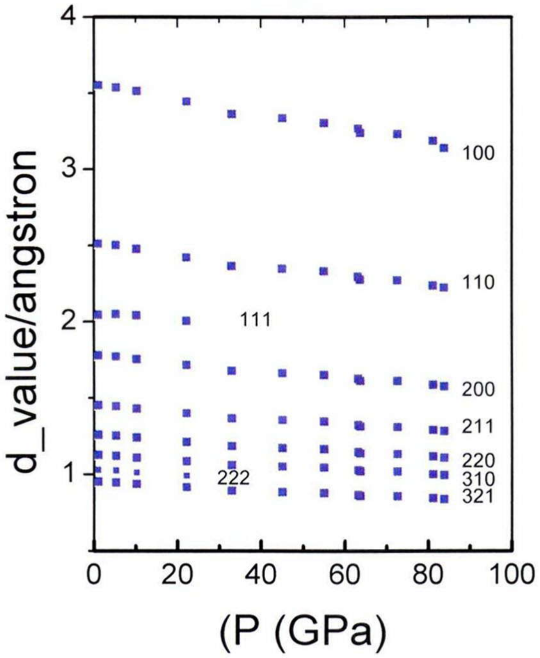

Fig. 4.13: The relationship between d-spaces and pressure.

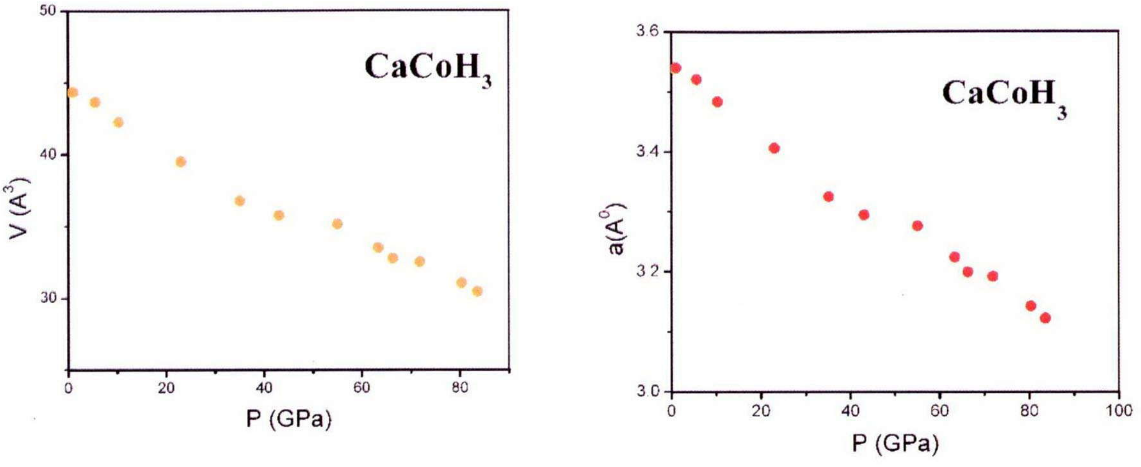

Fig. 4.14: The value as a function of pressure during compression.

The result is consistent with the aforementioned in situ measurement of resistance versus pressure. The vanish of d-spacing of peak (111) in the pressure range 33.5 -83 GPa does not result in a change of volume of the primitive unit cell V as shown in Fig. 4.14, which corresponds to the volume of one cubic cell of the initial Pm-3m phase because the d-values of the other peaks are decreasing with increasing pressure. It reveals that the cubic perovskite phase is stable in a wide range of high pressure, and no phase transition at room temperature to 83 GPa.

4.2.3 Metallization of $CaNiH_3$

Figure 4.15 shows the spectra of X-ray diffraction results of $CaNiH_3$ at various pressures. Indexing can be a cubic perovskite up to 62 GPa. There is also a vanished (111) peak at ~ 25 GPa. Comparing with $CaCoH_3$, the same in relative peak intensity attributed to the distortion of sample. The d-value and volume as a function of pressure is shown in Fig. 4.16 and Fig. 4.17, respectively. It is demonstrate that the most of transition metal in perovskite structure is usually very stable under high pressure.

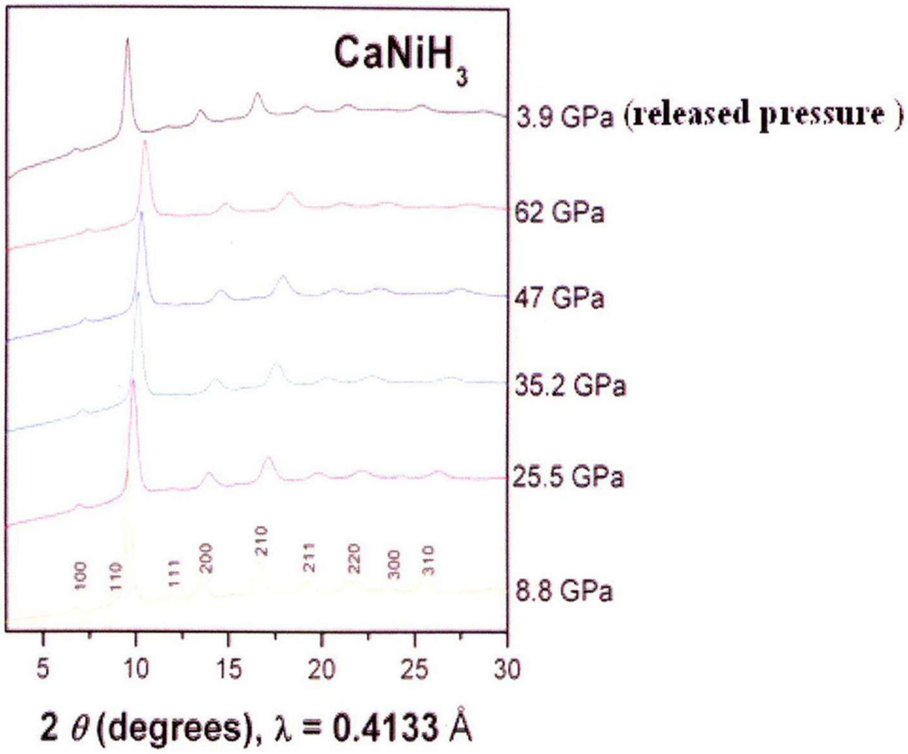

Fig. 4.15: X-ray diffraction patterns of CaNiH$_3$ at several pressures.

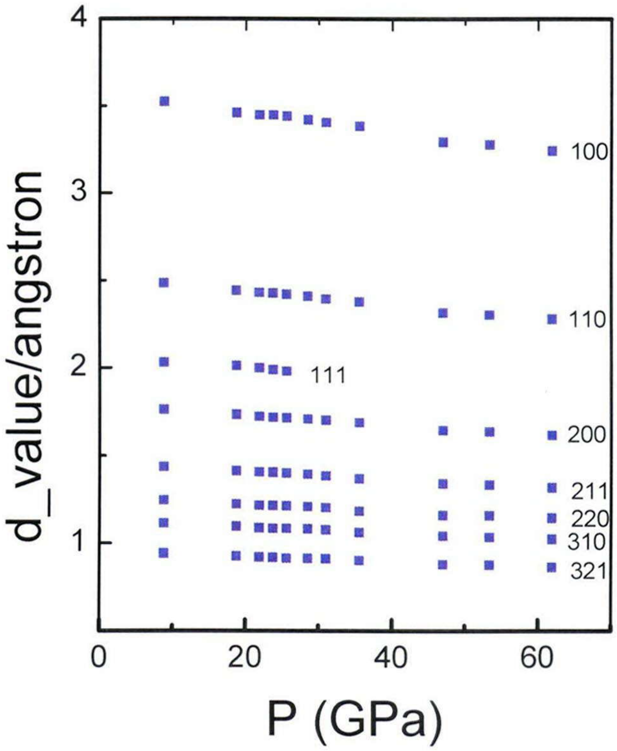

Fig. 4.16: The relationship between d-spaces and pressure.

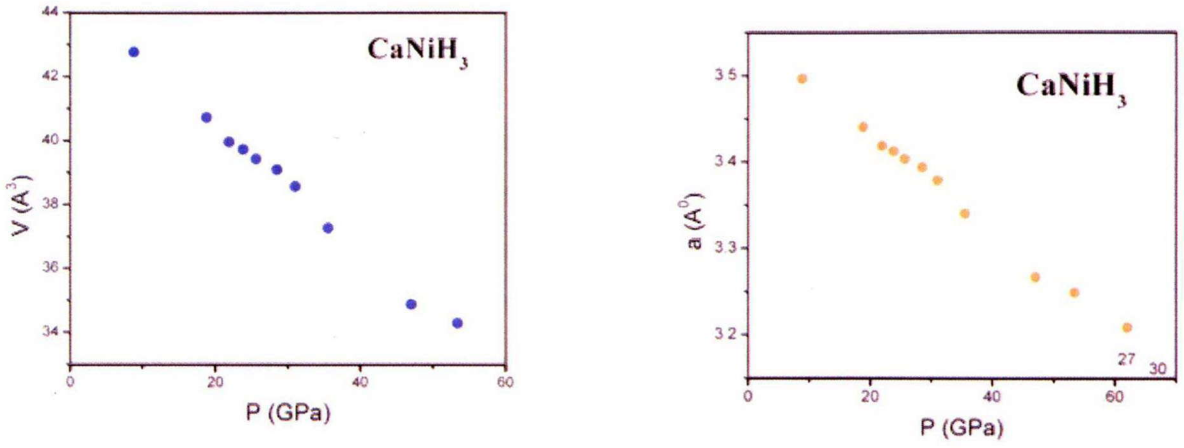

Fig. 4.17: The volume as a function of pressure during compression

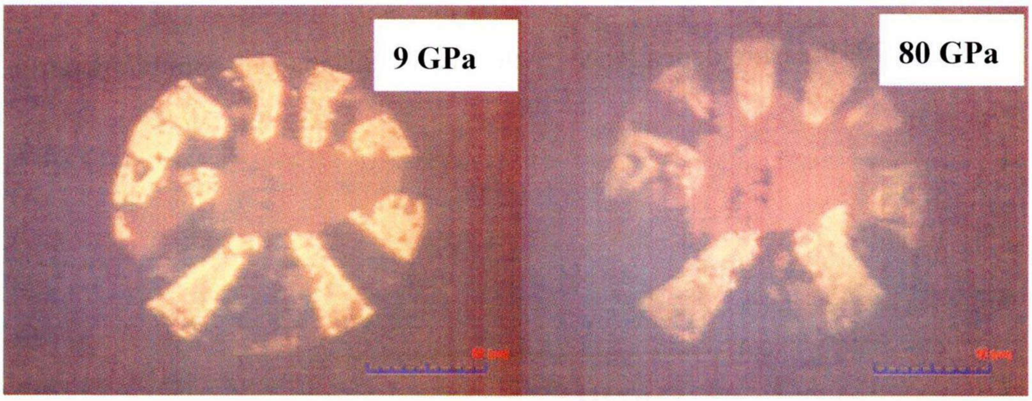

Fig. 4.18: The color changed from black to reddish brown a gain in CaNiH$_3$.

The color of the hydride was reddish brown. The lattice parameter was a = 0.35542 nm [19]. The color of the sample changed from black to reddish brown from 9 GPa up to 80 GPa as shown in Fig. 4.18. As show in Fig. 4.19, the resistance of the sample decreased up to ~ 25 GPa, and increase up to 90 GPa.

The temperature dependence of electrical resistance of the CaNiH$_3$ is shown in Fig. 4.20. The resistance decreased with decreasing temperature.at all pressures. These slope demonstrated the metallic character. With pressure increasing, the absolute value of resistance showed minima at 25 GPa. No superconductivity was observed. There show a typical semiconductor temperature increases the resistance at very low temperatures.

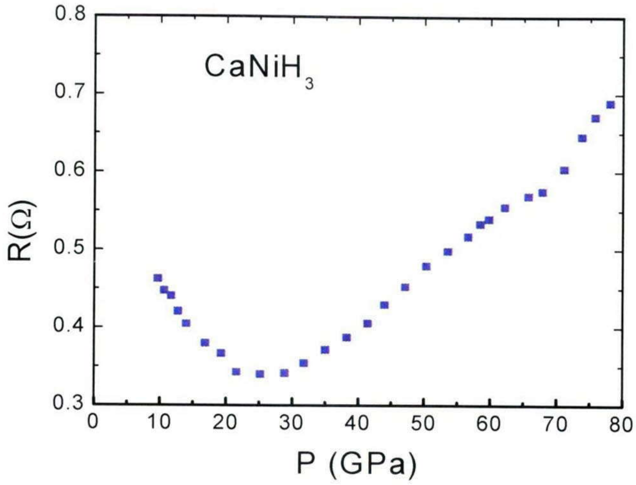

Fig. 4.19: Pressure dependence of electrical resistance at room temperature.

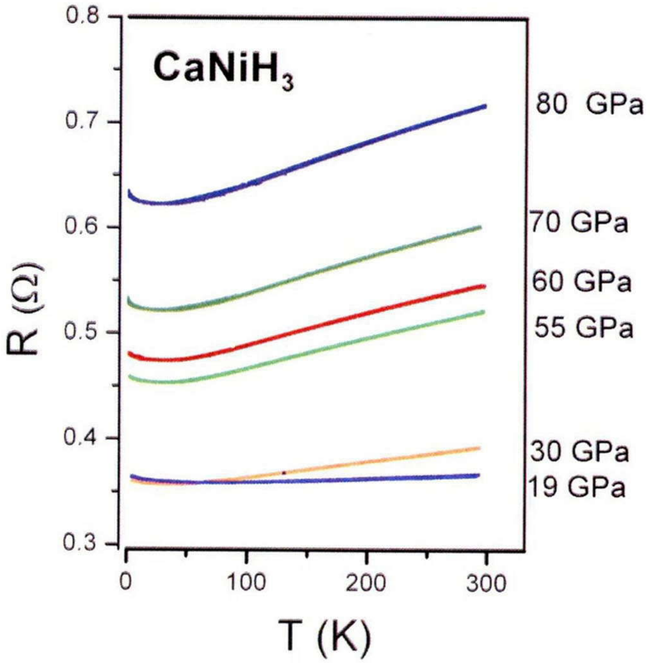

Fig. 4.20. Temperature dependence of electrical resistance at different pressures.

4.3 Summary

The temperature dependence of resistance shows metallic behavior indicating the onset of the metallic state in $CaCoH_3$ above 40 GPa. No superconductivity was observed. The cubic perovskite phase is stable in a wide range of high pressure, and no phase transition at room temperature.

References

[1] N.W. Ashcroft, Phys. Rev. Lett. 21, 1748 (1968).

[2] Eremets, Science. 2008 Mar 14;319(5869):1506-9.

[3] T. Sato Joural of Solid State Chemistry 178 (2005) 3381-3388

[4] K. Komiya Proceeding International Hydrogen Energy Congress and Aehibition IHEC 2005. Itanbul, Turkey. 13-15 July 2005

[5] W. Bronger Journal of Alloys and Compounds 229 (1995) 1-9

[6] L. Nakatsuka Journal of Alloys and Compounds 293-295 (1999) 222-226

[7] H. T. Takeshita, T. Oishi and N. Kuriyama, J Alloys Compd., 333 (2002), 266-273.

[8] H. T. Takeshita, T. Furuya, H. Miyamura and N. Kuriyama, Trans. Mater. Res. Soc. Japan,29 (2004), 2049-2051.H5-6

[9] T. Sato, D. Noréus, H. T. Takeshita and U. Häussermann, J. Solid State Chem., 178 (2005), 3381-3388.

[10] H. T. Takeshita, Y. Sakamoto, N. Takeichi, T. Kiyobayashi, H. Tanaka, N. Kuriyama, H.Senoh, J. Alloys Compd., 347 (2002), 231-238.

[11] Bouamrance et al,.. Material research Bulletin 35 (2000) 545-549

[12] P. Vajeeston et al,. Journal of Alloys and Compounds 450 (2008) 327-337

[13] K . Ikeda Scripta Materialia 55 (2006) 827–830

[14] K Ikeda et al, Int. J. Mat. Res (formerly Z. Metallkd) 99 (2008) 5

[15] K. Ikeda Progress in Solid State Chemistry 35 (2007) 329e337

[16] S. Orimo Progress in Solid State Chemistry 35 (2007) 329e337

[17] R. H. Mitchell: Perovskites, Modern and Ancient, Almaz Press Inc., Thnder bay (2002)

[18] F. S Galasso: structure and properties of inorganic solids, pergamon Press, Oxford (1970) 162

[19] H. Kakuta, Materials Transactions, Vol. 42, No. 3 (2001) pp. 443 to 445

Chapter 5. Conclusions

Purpose of this research is to search for a pressure-induced insulator to metal transition in hydrogen rich systems. Two systems are focused in this thesis. The first system is YH_3 and the second is perovskite hydrides $CaCoH_3$ and $CaNiH_3$, expecting as alternative approach to "metallic hydrogen".

This thesis was done as a part of survey of dense hydrogen for high-temperature superconductivity. The first part of the thesis derived the macroscopic properties of hydrogen and reviews on developed high-pressure technique to make it possible to routinely perform resistance measurements at high pressures.

Chapter 3 was for yttrium hydride. We have succeeded in synthesized the insulating transparent YH_3 samples by hydrogenation from yttrium metal in fluid H_2 under high pressure. Measurement of the electrical resistivity at high pressure and low temperature demonstrated an electronic phase transition from insulator to metal at around 70 GPa in the fcc phase.

In the Chapter 4, the perovskite hydride ($CaNiH_3$, $CaCoH_3$) is studied. Both samples reveal that the cubic perovskite phase is stable in a wide range of pressure, and no structure phase transition at room temperature to 62 GPa and 83 GPa, respectively. The temperature dependence of resistance shows metallic behavior indicating the onset of the metallic state in $CaCoH_3$ above 40 GPa. In the case of $CaNiH_3$, the onset pressure of metallization is 15 GPa. However, the superconductivity was not observed yet up to 80 GPa in both samples.

The improvements in technology through this thesis such as cryogenic hydrogen loading systems, will works for further metal hydrides; FeH_x, LaH_2, PdH, EuH_x, ScH_3 so on....

The result could be an important step towards understanding underlying physics of superconducting metallic hydrogen rich system by the picture of both materials, and provides a new system to study high temperature superconductivity.

Published works

Publication List (Including papers submitted, accepted and in print)

[1] Zhenhua Chi, **Huyen Nguyen**, Takahiro Matsuoka, Tomoko Kagayama, Naohisa Hirao,Yasuo Ohishi, and Katsuya Shimizu, "Cryogenic implementation of charging diamond anvil cells with H_2 and D_2", Review of scientific instruments 82, 105109 (2011)

[2] **Huyen Nguyen,** Zhenhua Chi, Takahiro Matsuoka, Tomoko Kagayama and Katsuya Shimizu, "Pressure-induced metallization and superconductivity of yttrium trihydride, YH_3", Supplimental issue of the Journal of Physical Society of Japan (unknow)

List of Oral or Poster Presentation in Domestic Meetings

[1] Development of cryogenic gas-loading system for metal hydride

G-COE siminar, 13-15 Nov 2008 (poster)

[2] Transport properties of YH_3 under high pressure and low temperature

the 6th 8 university PhD student exchange forum, 10-11 Sept (poster)

G-COE siminar , 14-16 Sep2009 (poster)

JPS 2009 Autumn Meeting 25-28 Sept 2009 (oral).

[3] High pressure effect on yttrium tri-hydride property.

Global COE Program, 2-3 March 2010 (oral)

[4] Pressure-induced insulator-metal transition of ABH_3 hydride

JPST 23-26 Sept 2010 (oral).

[5] High pressure effect on the property of perovskite hydrides, $CaNiH_3$ and $CaCoH_3$

Global COE Program, 28-30 Oct 2010 (oral)

[6] High pressure effect on the electrical and structural properties of perovskite hydrides $CaNiH_3$ and $CaCoH_3$

JPST 22-25 Sept 2011 (oral).

[7] Pressure-induced metallization in perovskite hydrides $CaNiH_3$ and $CaCoH_3$

Japan High Pressure conference, 8-12 Nov 2011 (oral)

Presentation in International Conferences

[1] Development of cryogenic gas-loading system for metal hydride

The 1st SNU-KYOKUGEN mini-symposium (10-2008) (poster)

[2] The pressure induced insulator-metal transition of yttrium tri-hydride (YH_3).

2nd SKLSHM-KYOKUGEN workshop, 8-11 Dec 2009 (poster).

[3] Pressure-induced electronic phase transition in Yttrium hydride.

5th JAEA Synchrotron Radiation Research Symposium conference 25-26 Feb 2010 (poster)

[4] Pressure induced insulator-metal transition of yttrium tri-hydride (YH_3)

GCOE-ICNDR conference, 30May-4June 2010 (poster)

[5] High pressure effect on property of perovskite hydrides, $CaNiH_3$ and $CaCoH_3$

5th Asian Conference on High Pressure Research, 8-12 Nov 2010 (poster)

[6] Pressure-induced electronic phase transition in yttrium hydride

2010 GRC on Research at High Pressure, 27 June-2July 2010 (poster)

Acknowledgements

This thesis was carried out in the Shimizu group of KYOKUGEN, Center for Quantum Science and Technology under Extreme Conditions in Osaka University and partly in SPring-8.

I would like to express the sincere gratitude to Professor Katsuya Shimizu, who is my supervisor of during my studying in Japan from April 2008, for his thoughtful guidance, encouragement, discussions and careful reading of this dissertation. I am very grateful to my supervisor for helping with the suggestion when I am facing problems with my study. My life at Japan would be much harder without his help. No word can replace my appreciation to him for his patiently checked through my manuscript, reports, and has shown me the attraction in high pressure research. I give special thanks to Prof. Hoang Dzung in National University of Hochiminh city for his comment and support my schedule of doctor course.

I especially express my thanks to Associate Prof. Tomoko Kagayama, for her detailed and constructive comments and important support throughout my research. The greatest thanks are due to Dr. Yuki Nakamoto for always encouraging and supporting and comments of the research work.

This is chance for me to praise to Dr. Masafumi Sataka for valueble suggestion, supportive wisdom and helping me in measurement. I would like to thank Dr. Zhenhua Chi for valuable assistance and helping in the fabrication of the samples and the experiments.

I am indebted to Assistant Professors Atsushi Miyake and Takahiro Matsuoka for their invaluable guidance, helpful discussions, and indefatigable help throughout this dissertation work. I would like to thank Professor Shin-ichi Orimo in Tohiku university for providing an interesting research samples.

This work is helped from our collaborators, especially thank to my present and past lab members for valuable group interactions, friendship and support. I would like to thank my friends for their help and friendship.

I give special thanks to Prof. Tadashi Itoh in Osaka Univerisy, Prof. Nguyen Xuan Phuc, Prof. Le Van Hong, Prof. Nguyen Quang Liem in Institute of Materials Science of Vietnamse Academy of science and technology for support my schedule of doctor course. I am very grateful to Ms. Emiko Tasaka, other member of the International student office and members office of KYOKUGEN for their help consideration and support. I give special thanks to Ms. Asako Yanagi, who is my Japanese teacher for her kindness as host family with her support during my life in Japan.

I would like to acknowledgement the Vietnamese Government, the Japanese Government, the 21st Century Center of Excellence for Materials Science and Nano Engineering, and the Global COE Program, Japan for grant of the scholarship during PhD program in Japan.

My special thanks to my mother and everyone in my family members, who have made my academic pursuit possible and financial support for my life and studies so far.

Once again, I would like to express my sincere gratitude all of you for your support. It has been of immense encouragement for my life in past and future.